J. Fluid Mech. (2001), *vol.* 441, *pp.* 67–108. Printed in the United Kingdom

© 2001 Cambridge University Press

Examination of large-scale structures in a turbulent plane mixing layer. Part 2. Dynamical systems model

By L. UKEILEY[1], L. CORDIER[2], R. MANCEAU[3], J. DELVILLE[3], M. GLAUSER[4] AND J. P. BONNET[3]

[1]National Center for Physical Acoustics, University of Mississippi, University, MS 38677, USA

[2]LEMTA UMR CNRS 7563, Vandoeuvre-lès-Nancy, France

[3]LEA/CEAT UMR CNRS 6609, Poitiers, France

[4]Department of Mechanical, Aerospace and Manufacturing Engineering, Syracuse University, Syracuse, NY 13244, USA

(Received 28 March 1998 and in revised form 12 February 2001)

The temporal dynamics of large-scale structures in a plane turbulent mixing layer are studied through the development of a low-order dynamical system of ordinary differential equations (ODEs). This model is derived by projecting Navier–Strokes equations onto an empirical basis set from the proper orthogonal decomposition (POD) using a Galerkin method. To obtain this low-dimensional set of equations, a truncation is performed that only includes the first POD mode for selected streamwise/spanwise (k_1/k_3) modes. The initial truncations are for $k_3 = 0$; however, once these truncations are evaluated, non-zero spanwise wavenumbers are added. These truncated systems of equations are then examined in the pseudo-Fourier space in which they are solved and by reconstructing the velocity field. Two different methods for closing the mean streamwise velocity are evaluated that show the importance of introducing, into the low-order dynamical system, a term allowing feedback between the turbulent and mean flows. The results of the numerical simulations show a strongly periodic flow indicative of the spanwise vorticity. The simulated flow had the correct energy distributions in the cross-stream direction. These models also indicated that the events associated with the centre of the mixing layer lead the temporal dynamics. For truncations involving both spanwise and streamwise wavenumbers, the reconstructed velocity field exhibits the main spanwise and streamwise vortical structures known to exist in this flow. The streamwise aligned vorticity is shown to connect spanwise vortex tubes.

1. Introduction

Understanding and modelling turbulent flows has become increasingly important as more advanced applications require knowledge of the finer details of the turbulence. At the same time it is becoming increasingly evident that large-scale organized motions present in turbulent flows influence many physical properties such as mixing, separation, noise, vibrations, heat transfer, drag, lift, etc. Therefore, understanding the dynamics of large-scale flow organization plays a crucial role in the ability to understand, predict and ultimately control turbulent flows. In that vein, the method offered in this study leads to a relatively simple dynamical model, in comparison to

https://doi.org/10.1017/S0022112001004803 Published online by Cambridge University Press

the full Navier–Stokes equations, which can be used as a tool for understanding the dynamics of the flow and serve as a test bed for control applications.

The idea of applying a low-order dynamical systems approach of the type discussed in this communication stems from the desire to simplify the Navier–Stokes equations to a minimal set of ordinary differential equations (ODEs), able to describe correctly the essential dynamical behaviour of the flow. The approach uses a small set of equations modelling some attractor (obtained through a truncation procedure based on the physics of a given flow) whose solutions have enough similar character to the solutions of the Navier–Stokes equations to capture the underlying physical processes. The lower dimension of the new system allows easier comprehension of the mechanisms in turbulence. The proper orthogonal decomposition (POD), first introduced in fluid mechanics by Lumley (1967), provides an optimal basis set in terms of kinetic energy representation; thus utilizing the eigenfunctions of the POD for the basis set can provide low-dimensional systems with a relatively small number of equations.

Lorenz (1963) was the first to utilize a low-order dynamical system to study fluid mechanics. Based on physical approximations, he developed a set of three first-order differential equations to model the temperature and velocity field dynamics in a Rayleigh–Bénard convecting layer. Some years later, Ruelle & Takens (1971) made the theoretical link between low-order dynamical systems and turbulence. They proposed that, in a certain bounded domain and under specific conditions, a mathematical object called a strange attractor which corresponds to turbulence might exist for the Navier–Stokes equations. This work led to many studies using dynamical systems techniques, especially for closed flow systems. The following is some of the work using POD–Galerkin models for open flow systems. For a more comprehensive list see Berkooz, Holmes & Lumley (1993*a*) or Delville (1995).

A low-order dynamical system based on POD modes was first applied to an open turbulent system by Aubry *et al.* (1988). They developed a low-dimensional set of ODEs that model the near-wall region of a turbulent boundary layer by using the experimentally determined eigenfunctions of Herzog (1986). Their model equations (hereafter called the Cornell model) exhibited several dynamical regimes (periodic, quasi-periodic, intermittent, chaotic) as the Heisenberg control parameter was varied. When the solutions of their model ODEs are used to reconstruct the three-dimensional velocity fields in the wall region, they found results consistent with experimental observations in a turbulent boundary layer, i.e. the burst–sweep cycle. For a full review of their findings in the context of dynamical systems the reader is referred to the book by Holmes, Lumley & Berkooz (1996).

Based on the initial work of Aubry *et al.* (1988), a significant number of other studies have been undertaken. Aubry, Lumley & Holmes (1990) modelled drag reduction on the wall region by applying stretching transformations to the eigenfunctions of the Cornell model. This study suggests that the intermittent events observed in the original model cannot be considered as an artifact of the closure assumption but are deeply rooted in the dynamical phenomena of the wall region. Berkooz, Holmes & Lumley (1991) generalized the wall layer Cornell model to permit uncoupled evolution of streamwise and cross-stream disturbances. Their main conclusion was that the intermittent behaviour reported in Aubry *et al.* (1988) is a direct consequence of the ODE's invariant subspaces and symmetries which reflect natural physical symmetries of the flow. Sanghi & Aubry (1993) investigated the persistence of the intermittent behaviour observed in the model of Aubry *et al.* (1988) when streamwise variations which were not accounted for in an explicit way in the Cornell model are

https://doi.org/10.1017/S0022112001004803 Published online by Cambridge University Press

now considered. With this higher-order model, the intermittent behaviour persisted, but with higher additional complexities.

Since the original work of the Cornell group, others have examined the role of coherent structures in the wall region of a turbulent boundary layer with a similar approach. To avoid introducing an inhomogeneous pressure term at the boundary as was done in the Cornell model, Zhou & Sirovich (1992) constructed 'wall' eigenfunctions with full channel validity. In order to facilitate comparisons with the results of the Cornell model, they first adopted the same severe truncation: five modes with no streamwise variation. This five-mode model equation displayed intermittent, quasi-periodic, and chaotic behaviour similar to that found by the Cornell group. When propagating modes (streamwise-dependent modes) are included in the model, a physically more realistic dynamical behaviour is then obtained. They concluded that the propagating modes lie more at the heart of the triggering mechanism for the bursting process than does the idea of pressure fluctuations proposed previously by Aubry *et al.* (1988). To get a better understanding of the final stages of transition in a boundary layer, Rempfer (1995) derived dynamical models for different regions of the flow, by Galerkin projection of the Navier–Stokes equations onto the POD eigenfunctions extracted from numerically computed flow fields.

Free shear flows have been studied using the POD–Galerkin type models in both jets and mixing layers. A low-order dynamical systems model was developed for the axisymmetric jet by Glauser, Zheng & Doering (1989) and Zheng & Glauser (1991). The eigenfunctions utilized in these studies have been extracted from two-point velocity measurements in the mixing layer of a high Reynolds number axisymmetric jet (see Glauser & George 1992 and Glauser 1987). Glauser, Zheng & George (1990) postulated a spatially evolving dynamical system model for the axisymmetric jet mixing layer. In this model, the mean velocity quantities would be solved simultaneously, thus resulting in equations of a different form from that of the temporally evolving case. Rajaee, Karlsson & Sirovich (1994) applied the snapshot form of POD to measurements obtained in a non-turbulent forced mixing layer. Since their flow was forced through phase aligning the measurements, they were able to compute the time dependence of the POD random coefficients directly by projection of the snapshots on the eigenfunctions and to compare them with the result of the low-dimensional model. They found good agreement between the model and the direct projection, serving as justification for the low-dimensional description.

This study is the continuation of the work presented in Delville *et al.* (1999) that discussed the experimental measurements and the results from applying the POD to the plane turbulent mixing layer. Using the POD modes found in that study, low-dimensional dynamical systems models are developed in this communication by utilizing a Galerkin projection of the POD eigenfunctions on the Navier–Stokes equations. Due to the orthogonality condition of the eigenfunctions, this yields an ODE for each streamwise/spanwise wavenumber pair retained in a given truncation. The results of two truncations are presented here. The first involves a very severe truncation utilizing one POD mode and seven streamwise wavenumbers and the second a less severe truncation based on one POD mode but several streamwise/spanwise wavenumber combinations. Both systems of modelled equations for the POD expansion coefficients are solved with and without feedback between the modelled POD expansion coefficients and the mean flow (feedback involves a cubic term similar to the Aubry *et al.* (1988) work). From the modelled time-dependent POD expansion coefficients, and the measured POD eigenfunctions, the low-dimensional velocity field is constructed and used to study the temporal

https://doi.org/10.1017/S0022112001004803 Published online by Cambridge University Press

dynamics of the mixing layer and comparisons made to experiment. We find that for both truncations, feedback between the modelled POD expansion coefficients and the mean flow is key to obtaining the proper range of amplitude of the modelled POD expansion coefficients. The very severe truncation results (which do not include spanwise wavenumbers) are not able to mimic the proper spectral distribution obtained from experiment but when spanwise wavenumbers are added, as in the less severe truncation, very good comparisons between experiment and model result exist.

2. Application of POD to the plane turbulent mixing layer

A brief discussion of the application of POD to the plane turbulent mixing layer follows. For more details the reader is referred to Part 1 of this work (Delville *et al.* 1999).

Lumley (1967) suggested that the coherent structure should be the deterministic structure $\psi_i(\boldsymbol{x}, t)$ having the largest mean-square projection on the velocity field $u_i(\boldsymbol{x}, t)$. Maximizing the mean-square projection via the calculus of variations leads to the following integral eigenvalue problem:

$$\int_{\mathscr{T}} \int_{\mathscr{D}} R_{ij}(\boldsymbol{x}, \boldsymbol{x}', t, t')\psi_j(\boldsymbol{x}', t')\,\mathrm{d}\boldsymbol{x}'\mathrm{d}t' = \lambda\psi_i(\boldsymbol{x}, t). \tag{2.1}$$

The symmetric kernel of this Fredholm integral equation is the velocity cross-correlation tensor R_{ij} defined by

$$R_{ij}(\boldsymbol{x}, \boldsymbol{x}', t, t') = \langle u_i(\boldsymbol{x}, t)u_j(\boldsymbol{x}', t')\rangle, \tag{2.2}$$

where the angle brackets denote the appropriate average for the problem under consideration (see § 3.1 for a discussion on the averaging method performed in the mixing layer).

If the vector field is statistically homogeneous or periodic in one or more spatial directions or stationary in time, the eigenfunctions become Fourier modes (Lumley 1970; George 1988), so that the harmonic decomposition can be used in these directions. In the mixing layer under study, the spanwise direction is homogeneous. As detailed in Delville *et al.* (1999), time is mapped to the streamwise direction through Taylor's Hypothesis; thus this direction is also treated as homogeneous. With these conditions, the eigenvalue problem (2.1) becomes

$$\int_{\mathscr{D}} \Psi_{ij}(x_2, x_2'; k_1, k_3)\Phi_j^{(n)}(x_2'; k_1, k_3)\,\mathrm{d}x_2' = \lambda^{(n)}(k_1, k_3)\Phi_i^{(n)}(x_2; k_1, k_3), \tag{2.3}$$

where $\Psi_{ij}(x_2, x_2'; k_1, k_3)$ is the cross-spectral tensor, defined as the streamwise and spanwise Fourier transform of the cross-correlation tensor. The above equation is solved to extract the eigenfunctions used in the models developed in the next section where the kernel is supplied via experiment.

As pointed out in Lumley (1967), the properties of the integral equation (2.3) are given by the Hilbert–Schmidt theory. One interesting property is that the eigenfunctions form a complete orthonormal set, which means that the Fourier transform in the x_1- and x_3-directions of the fluctuating field can be reconstructed in the following way:

$$\hat{u}_i(k_1, k_3; x_2, t) = (L_1L_3)^{1/2} \sum_{n=1}^{N_{POD}} a_{k_1,k_3}^{(n)}(t)\Phi_i^{(n)}(x_2; k_1, k_3). \tag{2.4}$$

In the above equation, $a_{k_1,k_3}^{(n)}(t)$ are the temporal POD expansion coefficients. This

https://doi.org/10.1017/S0022112001004803 Published online by Cambridge University Press

relationship can be transformed back into physical space by the two-dimensional Fourier transform defined by

$$u_i(x_1, x_2, x_3, t) = \int_{-\infty}^{+\infty} \int_{-\infty}^{+\infty} \hat{u}_i(k_1, k_3; x_2, t) \exp(+2\pi \mathrm{i}(k_1 x_1 + k_3 x_3)) \, \mathrm{d}k_1 \, \mathrm{d}k_3. \tag{2.5}$$

In (2.4), L_1 and L_3 are the spatial extent of the domain $\mathscr{D}$ in the x_1- and x_3-directions, respectively, and N_{POD} is the number of POD modes.

The POD expansion coefficients $a^{(n)}_{k_1,k_3}(t)$ are determined by

$$a^{(n)}_{k_1,k_3}(t) = \frac{1}{(L_1 L_3)^{1/2}} \int_{\mathscr{D}} \hat{u}_i(k_1, k_3; x_2, t) \Phi^{(n)*}_i(x_2; k_1, k_3) \, \mathrm{d}x_2. \tag{2.6}$$

The dynamical systems that are developed in the following sections are low-order models from which the temporal evolution of the POD expansion coefficients $a^{(n)}_{k_1,k_3}$ in (2.4) can be extracted. Such models are needed because the integral (2.6) cannot be solved unless the velocity field is measured simultaneously over the whole decomposition domain. In our experiments such data were not available. Experimentally, the full field measurements are extremely difficult to obtain although the recent work of Bonnet *et al.* (1994) and Citriniti (1996) have shown that it is becoming more feasible.

In the context of our deterministic dynamical models, the temporal coefficients now become deterministic functions of time and are considered as 'building blocks' for studying the temporal evolution of the large-scale structures.

3. Temporal dynamical equations

The derivations of the equations for the dynamical models are presented in this section. The method used here is similar to that of Aubry *et al.* (1988) and Glauser *et al.* (1989). This methodology has been documented in a recent monograph by Holmes *et al.* (1996). In our work, two sets of equations are derived with their differences stemming from the closure method for the mean streamwise velocity. In each case, the mean velocity is calculated from a Boussinesq approximation (see (3.3)). The first method (§ 3.2.1) yields a mean velocity which is calculated *a priori* and is held constant throughout the time integrations. In the second method (§ 3.2.2), a cutoff wavenumber is chosen and the contribution to the mean velocity from wavenumbers lower than this wavenumber are assumed to be steady, while the contribution from wavenumbers greater than the cutoff vary with time. The difference between these two methods will be presented below. The importance of a non-zero contribution to a time-dependent mean velocity has been documented in Holmes *et al.* (1996). Such a mechanism is critical in this study to obtain modelled POD expansion coefficients with the proper amplitude. The results in § 6, where the linear stability of the trivial solution is discussed, also show the need for such a mechanism.

3.1. *Momentum equations*

In the same manner as detailed in Berkooz, Holmes & Lumley (1993*b*) and Aubry *et al.* (1988), the equations will be derived by performing a spatial average in the x_1- and x_3-directions denoted by $\langle \bullet \rangle$:

$$\langle \bullet \rangle = \frac{1}{L_1 L_3} \int (\bullet) \, \mathrm{d}x_1 \mathrm{d}x_3. \tag{3.1}$$

https://doi.org/10.1017/S0022112001004803 Published online by Cambridge University Press

To derive the temporal dynamical equations, the first step is to perform a Reynolds decomposition of the Navier–Stokes equations ($u_i = \langle u_i \rangle + u_i'$ where $\langle u_i \rangle = U_i$). For an incompressible fluid, without body forces, the following equation is obtained:

$$\frac{\partial u_i'}{\partial t} + u_j' \frac{\partial u_i'}{\partial x_j} - \left\langle u_j' \frac{\partial u_i'}{\partial x_j} \right\rangle + u_2' \frac{\partial U_1}{\partial x_2} \delta_{i1} + U_1 \frac{\partial u_i'}{\partial x_1} = -\frac{1}{\rho} \frac{\partial p'}{\partial x_i} + \nu \frac{\partial^2 u_i'}{\partial x_j \partial x_j}. \tag{3.2}$$

The following two assumptions have been made in deducing (3.2) from the Navier–Stokes equations: (*a*) $U_3 \approx 0$, (*b*) $U_2 \approx 0$, which corresponds to a thin mixing layer assumption. The first assumption is explicitly forced by the symmetries applied to the experimental data. The second assumption has been examined and it was shown that the terms involving U_2 were small in comparison to the other terms kept in the model. Note that the mean velocity can depend on time so that $U_1 = U_1(x_2, t)$.

It is important at this point to briefly discuss a potential inconsistency in the way equation (3.2) is derived and its actual implementation using the empirical eigenfunctions. The experimental data used to obtain the eigenfunctions were obtained from time averaging as articulated in § 3 of Delville *et al.* (1999). Thus an overlap of the spatial average and the temporal average is possible. This problem has been discussed by others such as Aubry *et al.* (1988) and more recently Rempfer (2000). In the limit of an infinite-dimensional model of a flow that is homogeneous in the spatial coordinates and stationary in time the problem will disappear.

3.2. *Eddy viscosity representation*

In this section a relationship for the mean streamwise velocity given in (3.2) will be presented. This relation is necessary because, in our severely truncated system, the measured mean velocity profile will be incorrect. Since there is no direct way to represent the mean velocity in terms of the POD modes an eddy viscosity relationship will be used to balance the mean streamwise velocity with the Reynolds stress term, which can easily be written in terms of POD modes. Two different ways of representing Reynolds stresses in terms of the POD modes will be discussed thus introducing two different mean velocity closures (see § 3.2.1 and § 3.2.2). Assuming that the Reynolds stresses act like the viscous stresses, Boussinesq (1877) developed a relationship where the Reynolds stresses are directly proportional to the velocity gradient. This relationship can be written for the mean streamwise velocity as follows:

$$U_1(x_2) = -\frac{1}{\nu_e} \int_0^{x_2} \overline{u_1' u_2'} \, \mathrm{d}x_2' + U_1(0), \tag{3.3}$$

where the Reynolds stresses can be expressed in terms of the POD modes as

$$\overline{u_1' u_2'} = \sum_{i=1}^{N_{POD}} \int\int_{-\infty}^{\infty} \lambda_{k_1,k_3}^{(i)} \Phi_{1,k_1,k_3}^{(i)} \Phi_{2,k_1,k_3}^{(i)*} \, \mathrm{d}k_1 \, \mathrm{d}k_3. \tag{3.4}$$

In (3.3) ν_e is determined from the free shear layer model as formulated by Prandtl–Reichardt: $\nu_e = K \delta_w (U_a - U_b)$ where $U_a - U_b$ represents the velocity difference, δ_w is the vorticity thickness and the constant K is 0.01 for the mixing layer. This approximation forces a constant eddy viscosity across the layer. Although ν_e is not truly constant across the mixing layer, the value from this relationship was found to be approximately equal to the integral value of ν_e calculated from (3.3) using experimental data (see Ukeiley (1995)). In (3.3), $U_1(0)$ is set to be equal to $U_m = (U_a + U_b)/2$ to preserve the convection velocity of the experimental system in our model. In later

https://doi.org/10.1017/S0022112001004803 Published online by Cambridge University Press

sections it will be shown that this term is important for the spectral behaviour of our low-order system.

Before deriving the relationships used in this study, the concept of the mean velocity modulation by the turbulence should be introduced. It is well known that the mean gradient contributes to the turbulence through the production process. However, many researchers in turbulence also feel that turbulent velocities must affect the mean velocities in some way. Wick, Glauser & Ukeiley (1994) studied the effect of the presence of a coherent structure on the mean streamwise velocity profile by applying pseudo flow visualization on a turbulent axisymmetric jet mixing layer. They found that the presence or absence of a structure alters the mean velocity profile. Therefore, the present study seeks to incorporate feedback between the turbulence and the mean. Holmes *et al.* (1996) have already discussed the value of including feedback from the turbulence to the mean velocity. They stressed that in the dynamical model of Aubry *et al.* (1988) without any feedback the system grew unbounded. This result is similar to the one obtained from the model presented in § 7.

3.2.1. *No-feedback relationship*

In this approach, a steady mean velocity is calculated and its numerical value is used in (3.2). This value is calculated from the only modes kept in the truncation as follows:

$$\begin{aligned} U_1(x_2) &= -\frac{1}{\nu_e}\int_0^{x_2}\left[\sum_{i=1}^{N_{POD}}\int_{-k_{1T}}^{k_{1T}}\int_{-k_{3T}}^{k_{3T}}\lambda^{(i)}_{k_1,k_3}\Phi^{(i)}_{1,k_1,k_3}\Phi^{(i)*}_{2,k_1,k_3}\mathrm{d}k_1\mathrm{d}k_3\right]\mathrm{d}x_2' + U_1(0)\\ &\equiv U_{1F}(x_2), \end{aligned} \tag{3.5}$$

where k_{1T} and k_{3T} represent the largest streamwise and spanwise wavenumbers kept in the truncation and N_{POD} is set to one. Even though there is no mechanism for feedback between the turbulent and mean velocity, the amplitude of the mean velocity should be appropriately scaled for the severely truncated systems studied here. The system of equations is driven by the production term and, in order to prevent the unbounded growth, this term must be of the correct order.

3.2.2. *Filter relationship*

In this approach, the streamwise velocity (3.3) is split into a steady and time-dependent part by choosing cutoff wavenumbers in both directions k_1 and k_3. These cutoff wavenumbers (k_{1C} and k_{3C}) act as a filter point. The contribution to the mean streamwise velocity from wavenumbers less than the cutoff value in a given direction is considered to be the *steady* part of the mean. The contribution from wavenumbers greater than the cutoff values correspond to the *unsteady* part of the mean and acts to provides feedback between the turbulence and mean flow. The ensemble of the modes (k_1, k_3) less than the cutoff values is defined by $E^{C\leqslant} = \{k_1, k_3; |k_1| \leqslant k_{1C} \text{ and } |k_3| \leqslant k_{3C}\}$ and the set $E^{C>}$ is formed of the wavenumbers kept in the truncation but with wavenumbers greater than the cutoff values $E^{C>} = \{k_1, k_3; k_{1T} \geqslant |k_1| > k_{1C} \text{ and } k_{3T} \geqslant |k_3| > k_{3C}\}$. This technique of spectral decomposition is applied to the mean velocity profile to yield

$$U_1(x_2, t) = U_{1F}(x_2) + U_{1\,uns}(x_2, t). \tag{3.6}$$

$U_{1F}(x_2)$ is estimated using (3.5) with the modes $(k_1, k_3) \in E^{C\leqslant}$ and $U_{1\,uns}(x_2, t)$ can be

https://doi.org/10.1017/S0022112001004803 Published online by Cambridge University Press

written as

$$U_{1\,uns}(x_2,t) = -\frac{1}{(L_1L_3)v_e} \times \int_0^{x_2} \left[\sum_{i=1}^{N_{POD}} \iint_{(k_1,k_3)\in E^{C>}} a^{(i)}_{k_1,k_3}(t) a^{(i)*}_{k_1,k_3}(t) \Phi^{(i)}_{1,k_1,k_3}(x_2) \Phi^{(i)*}_{2,k_1,k_3}(x_2)\, \mathrm{d}k_1\, \mathrm{d}k_3 \right] \mathrm{d}x_2', \tag{3.7}$$

by taking into account (2.4).

Substituting (3.6) into (3.2) yields

$$\frac{\partial u_i'}{\partial t} + u_j' \frac{\partial u_i'}{\partial x_j} - \left\langle u_j' \frac{\partial u_i'}{\partial x_j} \right\rangle + u_2' \frac{\partial U_{1\,uns}}{\partial x_2}\delta_{i1} + U_{1\,uns}\frac{\partial u_i'}{\partial x_1} + u_2' \frac{\partial U_{1F}}{\partial x_2}\delta_{i1} + U_{1F}\frac{\partial u_i'}{\partial x_1} = -\frac{1}{\rho}\frac{\partial p'}{\partial x_i} + \nu \frac{\partial^2 u_i'}{\partial x_j \partial x_j}. \tag{3.8}$$

In this equation, a fixed portion of the mean streamwise velocity forces a constant (non-time-dependent) production term combined with a relationship allowing feedback between the turbulent and mean velocities at higher wavenumbers. In the limit as k_{1C} and k_{3C} go to zero, $U_{1F} \equiv 0$ and the entire mean velocity is unsteady. This limiting case is examined both in Ukeiley (1995) and in terms of linear stability analysis in § 6.

3.3. *Fourier transform and Galerkin projection*

Before the Galerkin projection is performed two steps must be taken. The first step is to take the two-dimensional Fourier transform of (3.8) and the second one is to expand the Fourier coefficients of the velocity in terms of POD modes using (2.4).

After the two previous operations were performed on the manipulated Navier–Stokes equations, a Galerkin projection was applied. As defined in Aubry *et al.* (1988), this projection is represented by the following inner product:

$$(N, \Phi^{(l)}) = \int_{\mathscr{D}} N_{i,k_1,k_3}(t,x_2)\Phi^{(l)*}_{i,k_1,k_3}(x_2)\,\mathrm{d}x_2 = 0, \quad l = 1,\ldots,N_{gal}, \tag{3.9}$$

where $N_{i,k_1,k_3}(t,x_2)$ represents the Fourier transform of the Navier–Stokes equations and N_{gal} the number of Galerkin modes kept in the dynamical system. To obtain the final equations, the orthogonality relationship of the eigenfunctions was applied:

$$\int_{\mathscr{D}} \Phi^{(n)}_{i,k_1,k_3}\Phi^{(l)*}_{i,k_1,k_3}\,\mathrm{d}x_2 = \delta_{nl}. \tag{3.10}$$

After some analytical manipulations, (3.8) can be rewritten in a general form as

$$\frac{\mathrm{d}a^{(n)}_{k_1,k_3}}{\mathrm{d}t}(t) = \sum_{m=1}^{N_{gal}} \Lambda^{(m)}_{k_1,k_3}\, a^{(m)}_{k_1,k_3}(t) + \sum_{p,q=1}^{N_{gal}} \sum_{k_1',k_3'} Q^{(p)(q)}_{k_1',k_3',k_1,k_3}\, a^{(p)}_{k_1',k_3'}(t)\, a^{(q)}_{k_1-k_1',k_3-k_3'}(t) + \sum_{p,q,r=1}^{N_{gal}} \sum_{k_1',k_3'} C^{(p)(q)(r)}_{k_1',k_3',k_1,k_3}\, a^{(p)}_{k_1',k_3'}(t) a^{(q)*}_{k_1',k_3'}(t) a^{(r)}_{k_1,k_3}(t) - \frac{1}{\rho}\int_{\mathscr{D}} \frac{\partial \hat{p}_{k_1,k_3}}{\partial x_i}\,\Phi^{(n)*}_{i,k_1,k_3}(x_2)\,\mathrm{d}x_2. \tag{3.11}$$

https://doi.org/10.1017/S0022112001004803 Published online by Cambridge University Press

Since the eigenfunctions are divergence free and the streamwise and spanwise directions are assumed to be homogeneous, the pressure term in (3.11) can be written as

$$\int_{\partial\mathscr{D}} \hat{p}_{k_1,k_3}(x_2)\Phi^{(n)*}_{k_1,k_3} \cdot \boldsymbol{n}\,\mathrm{d}S = [\hat{p}_{k_1,k_3}(x_2)\Phi^{(n)*}_{2,k_1,k_3}(x_2)]^{L_2}_{-L_2}, \tag{3.12}$$

where $\partial\mathscr{D}$ is the boundary domain and $\boldsymbol{n}$ the outer normal on $\partial\mathscr{D}$. It can be argued that the eigenfunctions go to zero at the outer region of the shear layer. Under these conditions one can write $\Phi^{(n)}_{2,k_1,k_3}(x_2) = 0$ at $x_2 = -L_2$ and $x_2 = L_2$ so that the pressure term is eliminated. Note that this is different from the near-wall study of Aubry *et al.* (1988) where the effect of the pressure term needed to be modelled.

In the following two subsections, the dynamical equations will be derived for the two different mean velocity closures introduced in § 3.2.1 and 3.2.2.

3.4. *No-feedback relationship*

For the no-feedback relationship, the expression (3.11) can be written in a simplified form as follows:

$$\frac{\mathrm{d}a^{(n)}_{k_1,k_3}}{\mathrm{d}t}(t) = \sum_{m=1}^{N_{gal}} (\Lambda^{1(m)}_{k_1,k_3} + \Lambda^{2(m)}_{k_1,k_3}) a^{(m)}_{k_1,k_3}(t) + \sum_{p,q=1}^{N_{gal}} \sum_{k'_1,k'_3} Q^{(p)(q)}_{k'_1,k'_3,k_1,k_3} a^{(p)}_{k'_1,k'_3}(t) a^{(q)}_{k_1-k'_1,k_3-k'_3}(t), \tag{3.13}$$

where the coefficients $\Lambda^{1(m)}_{k_1,k_3}$, $\Lambda^{2(m)}_{k_1,k_3}$ and $Q^{(p)(q)}_{k'_1,k'_3,k_1,k_3}$ are calculated from the POD eigenfunctions. The exact form of these coefficients is given in Appendix A.

The first two terms on the right-hand side of (3.13) are linear. The first, $\Lambda^{1(m)}_{k_1,k_3}$, is a direct result of the viscous diffusion term in (3.8) ($\nu\partial^2 u'_i/(\partial x_j \partial x_j)$). The second term $\Lambda^{2(m)}_{k_1,k_3}$ results from the production and convection terms (the first part comes from $u'_2(\partial U_1/\partial x_2)\delta_{i1}$ and the second one comes from the term $U_1 \partial u'_i/\partial x_1$ of (3.8) and contains the mean velocity calculated from (3.5)). The term $Q^{(p)(q)}_{k'_1,k'_3,k_1,k_3}$ is quadratic; it represents the fluctuation interactions and expresses the transfer of energy between the Fourier and POD modes in the dynamical system (terms $u'_j \partial u'_i/\partial x_j - \langle u'_j \partial u'_i/\partial x_j \rangle$ of (3.8)).

3.5. *Filter relationship*

In this approach expression (3.11) can be written as follows:

$$\begin{aligned}\frac{\mathrm{d}a^{(n)}_{k_1,k_3}}{\mathrm{d}t}(t) = &\sum_{m=1}^{N_{gal}} \left(\Lambda^{1(m)}_{k_1,k_3} + \Lambda^{2(m)}_{k_1,k_3}\right) a^{(m)}_{k_1,k_3}(t) \\ &+ \sum_{p,q=1}^{N_{gal}} \sum_{k'_1,k'_3} Q^{(p)(q)}_{k'_1,k'_3,k_1,k_3} a^{(p)}_{k'_1,k'_3}(t) a^{(q)}_{k_1-k'_1,k_3-k'_3}(t) \\ &+ \sum_{p,q,r=1}^{N_{gal}} \sum_{(k'_1,k'_3)\in E^{C>}} C^{(p)(q)(r)}_{k'_1,k'_3,k_1,k_3} a^{(p)}_{k'_1,k'_3}(t) a^{(q)*}_{k'_1,k'_3}(t) a^{(r)}_{k_1,k_3}(t).\end{aligned} \tag{3.14}$$

In this closure assumption, the linear term $\Lambda^{1(m)}_{k_1,k_3}$ is the same as the one in the no-feedback case (§ A.1). The second linear term $\Lambda^{2(m)}_{k_1,k_3}$ is similar to the one in (3.13) except now $\Lambda^{2(m)}_{k_1,k_3}$ uses the filtered mean streamwise velocity U_{1F} calculated using (3.5) with the modes $(k_1,k_3) \in E^{C\leqslant}$. The quadratic term $Q^{(p)(q)}_{k'_1,k'_3,k_1,k_3}$ is the same as

https://doi.org/10.1017/S0022112001004803 Published online by Cambridge University Press

in (3.13). The last term $C^{(p)(q)(r)}_{k'_1,k'_3,k_1,k_3}$ is cubic and is a result of the modelling of the mean velocity. One part comes from the term $u'_2(\partial U_{1\,uns}/\partial x_2)\delta_{i1}$ and the other one comes from $U_{1\,uns}\partial u'_i/\partial x_1$ in (3.8) where $U_{1\,uns}$ is calculated from (3.7). This term represents the interaction between the mean velocity and the turbulent fluctuations with the summations performed only over values greater than the filter setting and not the whole truncated domain. The cubic coefficients are shown in the Appendix, § A.2.

4. Turbulent viscosity model

Due to the rapid convergence of the POD modes (49% of the turbulent kinetic energy is contained in the first mode, Delville *et al.* (1999)), only the first POD mode will be used in the truncations. Hence, the superscript denoting POD mode will be dropped and the first POD mode can be assumed.

To further reduce the degrees of freedom of the dynamical system, the number of streamwise/spanwise wavenumber pairs kept in the model will be truncated as well. As a result of the POD/wavenumber truncation there is a need to account for the energy transfer between the modes kept and the truncated modes. In this study a Heisenberg spectral model (Hinze 1975) similar to that used by Aubry *et al.* (1988) and Glauser *et al.* (1989) is applied. In this approach, it is assumed that the small scales (neglected modes) remove energy from the larger ones (the modes kept) via the global viscous action of a kinematic turbulence viscosity ν_T. See Appendix B for details of the method to estimate ν_T.

On introducing the turbulent viscosity ν_T into the dynamical equations (3.11), they become

$$\frac{\mathrm{d}a_{k_1,k_3}}{\mathrm{d}t}(t) = \left[\left(1+\alpha\frac{\nu_T}{\nu}\right)\Lambda^1_{k_1,k_3} + \Lambda^2_{k_1,k_3}\right] a_{k_1,k_3}(t) + \sum_{k'_1,k'_3} Q_{k'_1,k'_3,k_1,k_3} a_{k'_1,k'_3}(t) a_{k_1-k'_1,k_3-k'_3}(t) + \sum_{k'_1,k'_3} C_{k'_1,k'_3,k_1,k_3} |a_{k'_1,k'_3}(t)|^2 a_{k_1,k_3}(t), \tag{4.1}$$

where $C_{k'_1,k'_3,k_1,k_3}$ is zero for the no-feedback case. The coefficient α controls the drain of energy to the neglected modes and, in the context of dynamical systems, can be considered a bifurcation parameter.

5. General properties of the ODEs and solutions

This section details some of the properties of the differential equations along with the properties of the numerical integrations.

5.1. *Symmetry properties*

To solve the equations derived in the previous section it will be necessary to map some quantities to negative wavenumbers using symmetry properties of the flow field. For the eigenfunctions the applied symmetries are based on the relationships for the cross-spectral tensor as shown in Cordier (1996). The following symmetries are used for the eigenfunctions:

$$\left.\begin{array}{lll} \Phi_{1,-k_1,-k_3} = \Phi^*_{1,k_1,k_3}, & \Phi_{2,-k_1,-k_3} = \Phi^*_{2,k_1,k_3}, & \Phi_{3,-k_1,-k_3} = \Phi^*_{3,k_1,k_3}, \\ \Phi_{1,-k_1,k_3} = \Phi^*_{1,k_1,k_3}, & \Phi_{2,-k_1,k_3} = \Phi^*_{2,k_1,k_3}, & \Phi_{3,-k_1,k_3} = -\Phi^*_{3,k_1,k_3}, \\ \Phi_{1,k_1,-k_3} = \Phi_{1,k_1,k_3}, & \Phi_{2,k_1,-k_3} = \Phi_{2,k_1,k_3}, & \Phi_{3,k_1,-k_3} = -\Phi_{3,k_1,k_3}. \end{array}\right\} \tag{5.1}$$

https://doi.org/10.1017/S0022112001004803 Published online by Cambridge University Press

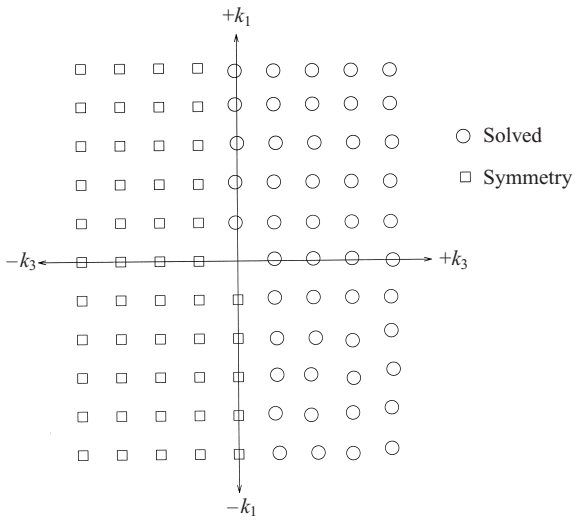


FIGURE 1. Solution domain.

The expansion coefficients $a_{k_1,k_3}(t)$ are instantaneous quantities, and there is no explicit reason why they should be forced to satisfy the above symmetries at all times. However, because the velocity is real, certain constraints can be imposed on these coefficients. Utilizing the symmetries on the eigenfunctions it can be shown that

$$a_{k_1,k_3}(t) = a^*_{-k_1,-k_3}(t). \tag{5.2}$$

5.2. *Solution domain*

For truncations involving several k_1 values with $k_3 = 0$, only positive values of k_1 are solved; the others are extracted from the application of the above symmetry to the *a*. When truncations involve wavenumbers of $k_3 \neq 0$ the solution expands dramatically. In these cases $\pm k_1$ is solved along with $+k_3$. The solution domain is graphically depicted in figure 1.

As the only symmetry involved relates the diagonal quadrants, the choice of solution domain is rather arbitrary. The solution domain could have easily been the inverse: $\pm k_3$ is solved along with $+k_1$. Checking this showed the domain solution chosen did not affect the solutions.

5.3. *The zero-wavenumber coefficient*

The zero-wavenumber mode ($k_1 = 0, k_3 = 0$) needs to be considered independently in the truncation. From (5.2), the coefficient $a_{0,0}$ is real and has a temporal evolution which is described by

$$\frac{\mathrm{d}a_{0,0}}{\mathrm{d}t} = \left(1 + \alpha\frac{v_T}{v}\right) \Lambda^1_{0,0} a_{0,0}, \tag{5.3}$$

where the coefficient $\Lambda^1_{0,0}$ is found numerically to be strictly negative.

Starting from (4.1), equation (5.3) can be obtained after the introduction of the following properties (see Appendix A for the expressions for the dynamical system coefficients):

(*a*) The factor $(1 - \delta_{k_1,0}\delta_{k_3,0})$ in front of the quadratic term in (A 3) implies that the contribution of this term is zero for the $(k_1 = 0, k_3 = 0)$ mode.

https://doi.org/10.1017/S0022112001004803 Published online by Cambridge University Press

(*b*) The cubic term in (A 3) is either equal to zero (for the no-feedback case) or is composed of two terms. In front of the first term, there is a factor $(2\pi ik_1)$, making this term equal to zero for $k_1 = 0$. In the second term the eigenfunction Φ_{2,k_1,k_3} appears causing it to be zero.

The continuity equation in the spectral domain can be written as

$$(2\pi ik_1)\Phi_{1,k_1,k_3}(x_2) + \frac{\partial}{\partial x_2}\Phi_{2,k_1,k_3}(x_2) + (2\pi ik_3)\Phi_{3,k_1,k_3}(x_2) = 0. \tag{5.4}$$

For $k_1 = k_3 = 0$, this equation becomes

$$\frac{\partial}{\partial x_2}\Phi_{2,k_1,k_3}(x_2) = 0,$$

and the eigenfunction $\Phi_{2,k_1,k_3}(x_2)$ is constant. We remind the reader that in § 3.3, we assumed that $\lim_{x_2\to\pm\infty}\Phi_{2,k_1,k_3}(x_2) = 0$; the consequence is that $\Phi_{2,k_1=0,k_3=0}(x_2) = 0$. Finally, the contribution of the cubic term in the feedback case is also equal to zero.

Equation (5.3) implies that the amplitude of the mode $a_{0,0}(t)$ decreases exponentially to zero with a time constant given by

$$\tau_{0,0} = -\frac{1}{(1+\alpha v_T/v)\Lambda^1_{0,0}}.$$

Therefore, this mode can only influence the dynamical evolution of the system for a short transient. (However, we have to keep in mind that for the very low values of the control parameter α, the time constant $\tau_{0,0}$ may be very high.) From now on, the amplitude of the coefficient $a_{0,0}(t)$ will be assumed to be zero, and the mode $(k_1 = 0, k_3 = 0)$ will not be retained in the truncation.

5.4. *Initial conditions*

The initial conditions for the system of equations are based on the magnitude of the eigenvalues. Essentially, since a goes like $(\lambda)^{1/2}$ the initial values for the coefficients will be determined by the following equation:

$$\mathrm{Re}\left(a^{(1)}_{k_1,k_3}(t=0)\right) = \mathrm{Im}\left(a^{(1)}_{k_1,k_3}(t=0)\right) = (\tfrac{1}{2}\lambda^{(1)}_{k_1,k_3})^{1/2} \tag{5.5}$$

where Re and Im denote the real and imaginary part of a complex number respectively. Using this value for the initial conditions the simulations should start with approximately the correct magnitude. In the discussion of the simulations this will help to serve as a criterion to evaluate the results.

The effects of varying the initial conditions have been studied and shown to have little effect on the results. A change in amplitude of the initial conditions, by as much as an order of magnitude, only affected the amount of time before the results settled into the same behaviour.

5.5. *Numerics*

To investigate the temporal evolution of the coefficients, a Runge–Kutta technique was utilized. The particular Runge–Kutta method used was a fifth/sixth-order Verner method from the IMSL numerical libraries. This particular method was chosen for ease of application along with its ability to multi-step between prescribed time steps. Several other Runge–Kutta methods were tried and shown to give the same quantitative results.

https://doi.org/10.1017/S0022112001004803 Published online by Cambridge University Press

A minimum time step of 8×10^{-5} s was chosen. This time step was used in order to minimize the intermittent stepping. Since for the truncations studied here one should not see frequencies greater than 1000 Hz, the selected step size allows adequate resolution of any waves observed.

Since the Runge–Kutta method used can only handle real-valued numbers, the coefficients are split into their real and imaginary parts,

$$a_{k_1,k_3}(t) = a^r_{k_1,k_3}(t) + \mathrm{i}a^i_{k_1,k_3}(t). \tag{5.6}$$

The number of degrees of freedom for the system then becomes twice the number of modes included in the system. Computationally this involved twice the number of equations; however, in the function evaluation for the Runge–Kutta method the real and imaginary parts were combined and complex manipulations were used.

For the three-dimensional simulations the spanwise and streamwise domains where $L_3 = 0.27\,\mathrm{m}$ and $L_1 = 0.345\,\mathrm{m}$ respectively. The spanwise domain is the physical domain of the experiments. It was shown by Delville *et al.* (1999) that the spanwise correlations had decayed within this window and in fact the spanwise spatial window is more than 3 integral scales in length. The streamwise domain contains at least two structures since the vorticity thickness is 28 mm and a typical structure has an aspect ratio 4 or 5.

The wavenumbers included in the system are defined as an integer times the experimental step $\delta k_{1\,exp} = \Delta f / U_c = 0.29\,\mathrm{m}^{-1}$ and $\delta k_{3\,exp} = \Delta k_z = 3.70\,\mathrm{m}^{-1}$ where Δf and Δk_z are, respectively, the minimal step size in frequency f and spanwise wavenumber k_z dictated by the experimental arrangement. From here on, only the integer value will be used and the appropriate δ will be assumed.

Computations were performed on an IBM RS6000 550 work station using double-precision arithmetic.

6. Linear stability analysis of the trivial solution

In this section, a linear stability analysis of the trivial solution for the general dynamical system (4.1) is performed. This analysis focuses on the influence of the mean streamwise velocity modelling and its effect on the dynamical behaviour of the system. Of special interest is the role of the different terms appearing in (3.13) for the no-feedback relationship and in (3.14) for the filter relationship.

The turbulent viscosity model introduced in Appendix B (see equation (B 5)) is a function of the specific truncation used in each low-dimensional system investigated. Hence, to give a general sense to the analysis, the viscous term $\alpha v_T / v$ in (4.1) was replaced for the analysis in this section by the term 100β, which is independent of the truncation under study. It follows from the definition of the turbulent viscosity, v_T, that the coefficient $1 + 100\beta$ is positive. Note that $\beta = -0.01$ corresponds to an inviscid configuration (Euler's equations).

6.1. *Analysis method*

Linearizing (4.1) around the trivial solution yields the following equations:

$$\left.\begin{aligned} \frac{\mathrm{d}r_{k_1,k_3}}{\mathrm{d}t} &= [(1+100\beta)\Lambda^{1,r}_{k_1,k_3} + \Lambda^{2,r}_{k_1,k_3}]r_{k_1,k_3}, \\ \frac{\mathrm{d}\theta_{k_1,k_3}}{\mathrm{d}t} &= [(1+100\beta)\Lambda^{1,i}_{k_1,k_3} + \Lambda^{2,i}_{k_1,k_3}], \end{aligned}\right\} \tag{6.1}$$

https://doi.org/10.1017/S0022112001004803 Published online by Cambridge University Press

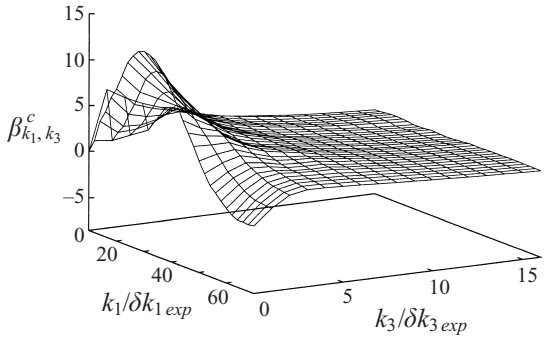


FIGURE 2. Marginal stability surface. No-feedback relationship.

where the complex number a_{k_1,k_3} is written in its polar form as $r_{k_1,k_3}e^{i\theta_{k_1,k_3}}$, and $\Lambda^{1,r}_{k_1,k_3}$, $\Lambda^{2,r}_{k_1,k_3}$, and $\Lambda^{1,i}_{k_1,k_3}$, $\Lambda^{2,i}_{k_1,k_3}$ are the real and imaginary parts of the terms $\Lambda^1_{k_1,k_3}$, $\Lambda^2_{k_1,k_3}$, respectively.

The linear stability of the trivial solution is directly determined by the sign of the linear growth rate defined as

$$\sigma_{k_1,k_3} = \mathrm{Re}(\Lambda_{k_1,k_3}) = (1 + 100\beta)\Lambda^{1,r}_{k_1,k_3} + \Lambda^{2,r}_{k_1,k_3}. \tag{6.2}$$

Note the following:

(i) if $\sigma_{k_1,k_3} < 0$, every harmonic disturbance is exponentially damped and the mode (k_1, k_3) is considered *stable*;

(ii) if $\sigma_{k_1,k_3} > 0$, every harmonic disturbance is exponentially amplified and the mode (k_1, k_3) is considered *unstable*;

(iii) if $\sigma_{k_1,k_3} = 0$, the mode (k_1, k_3) is considered *marginally stable*.

Regardless of the mode (k_1, k_3) under analysis, it has been found numerically that $\mathrm{Re}(\Lambda^1_{k_1,k_3}) < 0$, based on the assumption that when $\mathrm{Re}(\Lambda^2_{k_1,k_3})$ has negative values the linear growth rate σ_{k_1,k_3} remains negative for all values of the control parameter β. On the other hand, in the case where $\mathrm{Re}(\Lambda^2_{k_1,k_3})$ is positive, a critical value of β ($\beta^c_{k_1,k_3}$) can be found from the following relationship such that the linear growth rate becomes equal to zero:

$$\beta^c_{k_1,k_3} = -\frac{1}{100}\left(\frac{\mathrm{Re}(\Lambda^2_{k_1,k_3})}{\mathrm{Re}(\Lambda^1_{k_1,k_3})} + 1\right). \tag{6.3}$$

Thus for $\beta > \beta^c_{k_1,k_3}$ the mode (k_1, k_3) is *stable*, for $\beta < \beta^c_{k_1,k_3}$ the mode (k_1, k_3) is *unstable* and for $\beta = \beta^c_{k_1,k_3}$ the mode (k_1, k_3) is *marginally stable*.

6.2. *No-feedback relationship*

For the no-feedback relationship, a steady mean velocity profile $U_1(x_2)$ is used to close the system of equations (see § 3.2.1).

6.2.1. *Linear growth rate*

Figure 2 displays the surface of marginal stability determined using (6.3). Several observations can be made:

(*a*) when β is sufficiently high, all the modes (and thus the trivial solution) are stable;

(*b*) as β decreases, the marginal stability surface is intersected by the β-plane at a particular mode (k_1, k_3), which is considered to be *the most unstable mode*;

https://doi.org/10.1017/S0022112001004803 Published online by Cambridge University Press

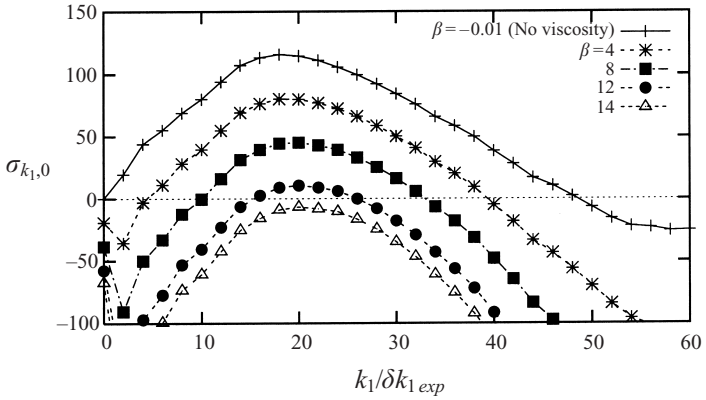


FIGURE 3. Linear growth rate of the two-dimensional modes ($k_3 = 0$) for several values of the control parameter β. No-feedback relationship.

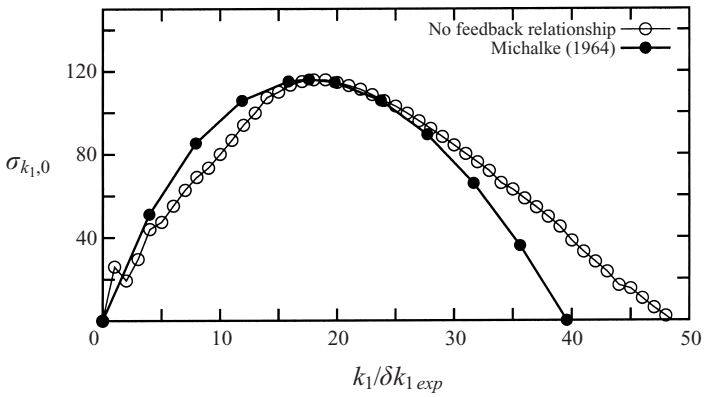


FIGURE 4. Linear growth rate of the inviscid turbulent plane mixing layer. No-feedback relationship.

(*c*) as β decreases further, there is an ensemble of modes (k_1, k_3) that are unstable;

(*d*) the most unstable modes are found for $k_3 = 0$ (two-dimensional modes), which is in agreement with the Squire theorem.

Further study in this section will be restricted to $k_3 = 0$ since it contains the most unstable mode. The evolution of the linear growth rate versus the non-dimensional streamwise wavenumber $k_1/\delta k_{1\,exp}$ is plotted in figure 3 for different values of the control parameter β. When $\beta = 14$, the linear growth rate is negative for all values of k_1. This implies that all of the modes are stable and hence the trivial solution is also stable. As β decreases the curve translates to larger ordinant values. The streamwise wavenumber $k_1/\delta k_{1\,exp} \simeq 20$ is the first mode to cross the horizontal axis of marginal stability; thus it is the most unstable mode and becomes unstable at $\beta \simeq 13.2$.

Figure 4 compares the linear growth rate obtained for an inviscid mixing layer by Michalke (1964) to that obtained using the simplified dynamical system ($\beta = -0.01$) presented in this work. An excellent agreement between the two curves can be observed for both the most linearly unstable mode k_1^{max} and the value of its linear growth rate. Unlike the study of Poje & Lumley (1995) where the maximum energy growth modes could be compared with the empirical eigenfunctions given by POD, the stability modes obtained by Michalke cannot be directly compared to the eigenfunctions of the current study. However, the eigenfunctions obtained by POD when only the

https://doi.org/10.1017/S0022112001004803 Published online by Cambridge University Press

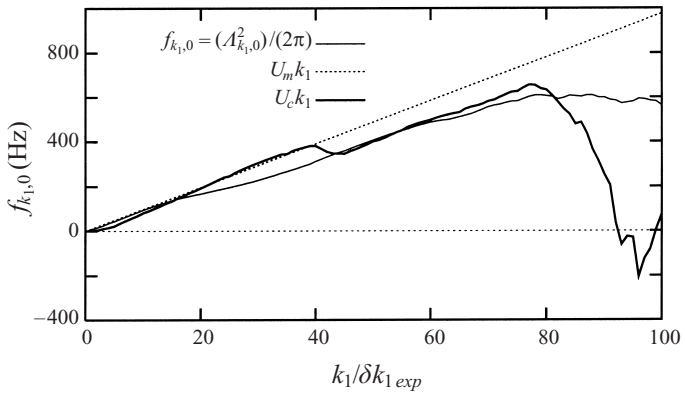


FIGURE 5. Frequencies of the low-order dynamical system. No-feedback relationship.

streamwise component of the velocity is retained exhibits the same types of symmetries as those determined by Michalke, i.e. the real part is even while the imaginary part is odd. Note that this result is consistent with the study of Rempfer & Fasel (1994) where they found in the case of a flat-plate boundary layer that the Karhunen–Loéve eigenfunctions of the POD and the Orr–Sommerfeld eigenfunctions of linear stability theory were almost identical when correctly normalized. The similarity between the two results is quite remarkable considering Michalke (1964) addressed the stability of the velocity profile while here the dynamical system is obtained via projection of the Navier–Stokes equations on the POD eigenfunctions which are based on the two-point correlation tensor. This point confirms that the first POD mode is not only pertinent in terms of energy content but also in terms of describing linear stability. These results suggest that a low-order dynamical system based only on the first POD mode could be used to clarify the flow mechanisms responsible for the dynamics of the large-scale structures.

6.2.2. *Spectral behaviour*

Applying (6.1), the frequency of a given two-dimensional mode $(k_1, 0)$ can be estimated in a first approximation†, as

$$f_{k_1,0} = \frac{\mathrm{Im}(\Lambda_{k_1,0})}{2\pi} = \frac{\mathrm{Im}\left[(1+100\beta)\Lambda^1_{k_1,0} + \Lambda^2_{k_1,0}\right]}{2\pi}. \tag{6.4}$$

This equation shows how $f_{k_1,0}$ is explicitly a function of the control parameter β. However, the coefficient $\mathrm{Im}(\Lambda^1_{k_1,0})$ was found numerically to be nine orders of magnitude smaller than $\mathrm{Im}(\Lambda^2_{k_1,0})$. Hence, 6.4 could be reduced to $f_{k_1,0} = \mathrm{Im}(\Lambda^2_{k_1,0})/2\pi$ without seriously altering the solution. Figure 5 represents the evolution of this frequency function with respect to $k_{1,0}$.

Michalke (1964) demonstrated that when the mean velocity profile is antisymmetric with respect to $y = 0$, the phase velocity of the instabilities is independent of k_1 and equal to $U_1(0)$. In a fixed frame of reference, these instabilities are convected by the flow and move at frequency of $U_m k_1$. Figure 5 shows that the frequency determined with the current dynamical system coincides with those estimated by Michalke. This result can be viewed as *a posteriori* justification of using $U_1(0) = U_m$ as the mean velocity profile in (3.3).

† The behaviour of the full dynamical system is not exactly this because, through the intermediary of the quadratic terms, the mode $(k_1, 0)$ is influenced by the other modes.

https://doi.org/10.1017/S0022112001004803 Published online by Cambridge University Press

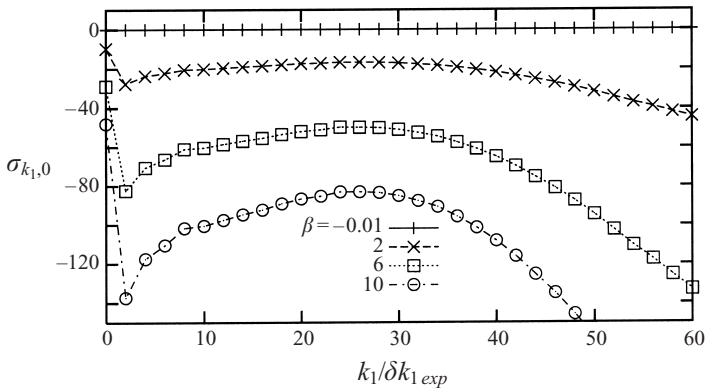


FIGURE 6. Linear growth rate of the two-dimensional modes ($k_3 = 0$) for several values of the control parameter β. (For $\beta = -0.01$ no viscosity.) Feedback relationship.

Lastly, in figure 5 the evolution of $U_c k_1$ is represented versus k_1 where U_c is the flow convection velocity determined in Delville *et al.* (1999). When compared to $\mathrm{Im}(\Lambda^1_{k_1,0})/2\pi$, $f_{k_1,0}$ is found to be better described by $U_c k_1$ than by $U_m k_1$. This result is particularly true in the interval $[50, 80]$ where U_c exhibits a constant value equal to $0.8U_m$ (Delville *et al.* 1999).

6.3. *Feedback relationship, $k_{1C} = k_{3C} = 0$*

For the feedback relationship, the mean velocity profile is decomposed into a steady part $U_{1F}(x_2)$ and an unsteady part $U_{1\,uns}(x_2, t)$ (see § 3.2.2). When $k_{1C} = k_{3C} = 0$, the steady part of the mean velocity profile reduces to $U_1(0) = U_m$, which implies that the linear term $\Lambda^2_{k_1,k_3}$ (defined in the Appendix, § A.1) may be simplified to the following:

$$\Lambda^2_{k_1,k_3} = -(2\pi \mathrm{i} k_1) U_m. \tag{6.5}$$

Note that $k_{1C} = k_{3C} = 0$ constitutes the limiting case of the feedback relationship where all the modes retained in the truncation contribute to the mean velocity in a time-dependent fashion.

6.3.1. *Linear growth rate*

Since the linear term $\Lambda^2_{k_1,k_3}$ is purely imaginary and given that $\mathrm{Re}(\Lambda^1_{k_1,k_3}) < 0$ for all (k_1, k_3), it was found that the trivial solution is stable. Figure 6 presents the linear growth rate for several values of the control parameter β for the most unstable modes ($k_3 = 0$). In this case, the marginal stability curve reduces to the plane where $\beta^c_{k_1,k_3} = -0.01$.

6.3.2. *Spectral behaviour*

In this section the analysis is restricted to the most unstable modes $k_3 = 0$. The frequency $f_{k_1,0}$ is still defined by (6.4) where, for the same reason as in § 6.2.2, the contribution of the linear term $\Lambda^1_{k_1,0}$ can be neglected. As was discussed earlier, the frequency can be approximated as

$$f_{k_1,0} = \frac{\mathrm{Im}\,(\Lambda^2_{k_1,0})}{2\pi} = U_m k_1, \tag{6.6}$$

and similar results to those presented in § 6.2.2 are found.

https://doi.org/10.1017/S0022112001004803 Published online by Cambridge University Press

6.3.3. *Global stability*

In § 6.3.1, it was demonstrated that the trivial solution is linearly stable, i.e. whatever the control parameter β, when the numerical integrations start with low-amplitude initial conditions then the solutions of the dynamical system tend to the trivial solution as $t \longrightarrow +\infty$. This result was confirmed by a numerical bifurcation analysis of the system under study (Cordier 1996). Using the bifurcation package AUTO94 developed by Doedel, Keller & Kernevez (1991), no other branch of the solution, even unstable, was found to bifurcate from the trivial solution. Hence assuming (all the numerical integrations that have been done confirm this assumption) that the low-order dynamical system (4.1) could not exhibit an isolated branch then the long-term evolution of the system is either the trivial solution or one which has unbounded growth to infinity. If the cubic term of the low-order dynamical system was negative the same argument as in Aubry *et al.* (1988) could be used to prove that the solutions would converge to zero (the system would be called *globally stable*). Unfortunately, contrary to the original study of Aubry *et al.* (1988), this is not the case here. The global stability of the system is not assured and some initial conditions could lead the solution to a diverge to infinity. Note that at this point it has not been shown that the system is globally stable, nor the opposite. However, since some initial conditions have been found to cause unbounded growth, it can be concluded that the basin of attraction of the trivial solution does not cover the space of all the initial conditions.

6.4. *Conclusion*

When the no-feedback relationship is used to close the dynamical equations, qualitative linear stability behaviour comparable to that reported by Michalke (1964) was obtained. However, the cubic terms are zero, allowing no feedback from the turbulence to the mean velocity. Thus for this closure, the growth of the perturbations does not reduce the slope of the mean velocity profile as was the case in the original study of Aubry *et al.* (1988).

On the other hand, the feedback relationship closure equation with $k_{1C} = k_{3C} = 0$ yields results that either converge to the trivial solution (linearly stable) or grow unbounded to infinity leading to an unphysical behaviour. In this specific case, even though our system is not globally stable, the cubic terms are non-zero, allowing some feedback from the turbulence to the mean velocity. When $k_{1C} \neq 0$ and/or $k_{3C} \neq 0$, the linear term $\Lambda^2_{k_1,k_3}$ is no longer purely imaginary (see (A 2)) and linearly unstable modes (k_1, k_3) could appear for the trivial solution.

The considerations mentioned above show the justification for the filter technique (with $k_{1C} \neq 0$ and/or $k_{3C} \neq 0$) to obtain behaviour compatible with linear stability theory results and to allow for feedback from the turbulence to the mean velocity.

7. Solution for truncations with $k_3 = 0$

Simulations of (4.1) using both the no-feedback relationship and the filter technique for $k_3 = 0$ are presented in this section. Two truncations were performed. The first, detailed in this paper, involved seven streamwise wavenumbers and one POD mode. In the second truncation, the system was reduced to include only five streamwise wavenumbers and one POD mode while the domain L_1 remained the same. This second truncation was studied in Ukeiley (1995) and will not be presented here. The five-mode system has very similar dynamics to the seven-mode system presented here. This is important since the truncations which involve non-zero spanwise wavenumbers

https://doi.org/10.1017/S0022112001004803 Published online by Cambridge University Press

(k_1, k_3)	$a_{k_1,k_3}(t=0)$
(10, 0)	$7.60000\,10^{-03}$
(20, 0)	$1.13771\,10^{-02}$
(30, 0)	$1.72755\,10^{-02}$
(40, 0)	$2.06431\,10^{-02}$
(50, 0)	$1.72524\,10^{-02}$
(60, 0)	$8.79664\,10^{-03}$
(70, 0)	$5.00210\,10^{-03}$

TABLE 1. Wavenumber pairs and initial conditions for the seven-mode model.

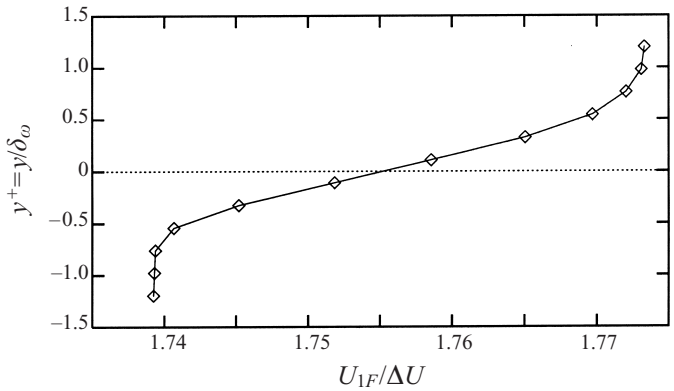


FIGURE 7. Mean streamwise velocity for seven-mode no-feedback simulations.

presented in § 8 only include five streamwise wavenumbers. This helps keep the system relatively small as non-zero spanwise wavenumbers are added to the system.

The seven-mode model described here was developed to provide some insight into the use of the filter technique for a small system before expanding to larger systems which include spanwise modes. It is also a useful two-dimensional limit (in wavenumber space) for comparisons to the simulations which include non-zero spanwise wavenumbers.

7.1. *Seven-mode model, no-feedback*

In this truncation with no non-zero spanwise wavenumbers included ($k_3 = 0$ only), the streamwise spacing is $10 \times \delta k_{1\,exp}$. The streamwise wavenumbers are the modes $k_1 =$ 10, 20, 30, 40, 50, 60, 70. Table 1 shows the initial conditions used for the simulation.

Note that the mean streamwise velocity used in (4.1) is not the measured quantity, but rather that calculated from (3.5). For the particular truncation studied here the integration in k_1 runs from 10 to 70. Figure 7 shows the mean velocity profile used for these simulations. In this figure and the ones to follow, x_2/δ_ω will be denoted by y^+. When comparing the profile in figure 7 to the measured values (see Delville *et al.* 1999), it is obvious that the convection velocity is preserved; however, the magnitudes on the low- and high-speed sides are significantly larger and smaller, respectively. This scales the production term, since it is dependent on the gradient of the mean streamwise velocity.

https://doi.org/10.1017/S0022112001004803 Published online by Cambridge University Press

(k_1, k_3)	(10, 0)	(20, 0)	(30, 0)	(40, 0)	(50, 0)	(60, 0)	(70, 0)
Frequency (Hz)	98.9	196.6	294.4	392.0	489.6	587.6	685.1

TABLE 2. Fundamental frequency for wavenumber pairs in the seven-mode system.

7.2. *Dynamics as a function of* α

Before discussing the dependence of the modelled POD expansion coefficients on α we will consider behaviour that occurs for all values of α examined. There is an underlying periodic (sinusoidal) behaviour that exists for all modes in the truncation. The frequencies of this behaviour depend on the streamwise wavenumber and are shown in table 2.

This periodic behaviour is always buried in the time traces of the coefficients, at some scale, regardless of what larger-amplitude events may be in the time series. The frequency increases with larger values of k_1. Since frequency is mapped to streamwise wavenumber through Taylor's Hypothesis, this seems intuitively correct. The values of the frequency obtained from the simulations for each streamwise wavenumber, as tabulated in table 2, vary by less than 0.5% from the frequencies used in the application of Taylor's Hypothesis.

Other complex behaviour, which will be discussed in further detail later in this section, sits on top of the underlying periodicities. Rajaee *et al.* (1994) obtained similar behaviour in a forced plane mixing layer where the results showed their coefficients exhibiting a complex behaviour on top of underlying periodicities.

The other behaviour that is observed regardless of the value of α is that the time-dependent POD expansion coefficient associated with mode (20, 0) appears to lead the temporal evolution, i.e. the coefficient has a larger magnitude and tends to be the first to increase or decrease as a function of time (see figure 8). This is consistent with the results discussed in § 6 where this mode was found to be the most unstable from the linear analysis. It is interesting to note that these results are also in agreement with the work done by Michalke (1964) using a hyperbolic tangent profile mixing layer. It is also interesting to note that this streamwise wavenumber is associated with energy in the centre of the mixing layer (see Delville *et al.* 1999). This behaviour is also similar to the results of Metcalfe *et al.* (1987), where it was postulated that disturbances from the centre of the mixing layer drive the instabilities that cause the flow to exhibit three-dimensionality.

An interesting inconsistency between this dominance of the coefficient associated with mode (20, 0) and the initial conditions used needs to be noted. As table 1 shows, the initial conditions associated with coefficients (30, 0), (40, 0), and (50, 0) have greater amplitude than the coefficient associated with (20, 0) (note that the initial conditions are obtained directly from the experimental eigenvalues). The results of the seven-mode simulation however, do not show this, and specifically, the modelled POD coefficients for modes (40, 0) and (50, 0) decay to zero while the (20, 0) coefficient remains finite. This is due to the lack of non-zero spanwise modes in the truncation. The two-dimensional ($k_3 = 0$ only) simulations do not allow for correct energy transfer from (20, 0) to the higher modes. In the three-dimensional (k_3 non zero) simulations presented in § 8, the modelled POD expansion coefficients associated with modes (40, 0) and (50, 0) do not decay to zero in general and their RMS time-averaged amplitudes are of the same order as that of the (20, 0) coefficient.

https://doi.org/10.1017/S0022112001004803 Published online by Cambridge University Press

Value of α	Behaviour
$\alpha < 1.55$	All modes grow unbounded to infinity
$1.55 < \alpha < 1.75$	Complex behaviour in full space
$1.8 < \alpha < 2.0$	Intermittent/complex periodic behaviour for all modes
$2.05 < \alpha < 2.45$	Periodic behaviour
$\alpha > 2.5$	Trivial solution

TABLE 3. Description of dynamics for seven-mode no-feedback model.

Table 3 outlines the typical dynamic behaviour for the seven-mode system at different values of the bifurcation parameter α. For values of α less than 1.55 the system is unstable and the solutions grow to infinity. In this range of α, the term A^2 linked to production grows at a rate which the dissipation term A^1 cannot overcome. This suggests that some feedback is necessary. As will be seen in § 7.6 feedback eliminates this problem. For $\alpha > 2.5$, the behaviour is the opposite, i.e. the global attractor for the system is a trivial solution. This means that all the modelled POD expansion coefficients decay to zero. Most of the coefficients decay at a similar rate except for the $(20, 0)$ coefficient which takes substantially longer to decay.

For α in the range of $2.05 < \alpha < 2.45$ the modelled POD expansion coefficients exhibit periodic behaviour. The time histories (0.4 s in total length) of the real and imaginary parts of the modelled coefficients are displayed in figure 8 for $\alpha = 2.2$. The results are typical of the behaviour of the system in this range of α. These time traces can be described as two sinusoids superimposed on each other. The first corresponds to an underlying streamwise-wavenumber-dependent frequency, while the second varies with α for all modes. Increasing α decreases the amplitude associated with the second frequency. As discussed earlier, the $(20, 0)$ coefficient always triggers the secondary frequency as it transfers energy to the higher modes. Also as mentioned earlier, for streamwise wavenumbers greater than 30, the amplitude of the oscillations is small, generally an order of magnitude less than the initial condition, while for streamwise wavenumbers less than 30, the amplitude of the modelled POD expansion coefficients tends to be of the same order as the initial conditions.

For $1.8 < \alpha < 2.0$ the system exhibits intermittent periodic behaviour. The solutions have a complex secondary periodic behaviour superimposed on the underlying periodicities. The modelled POD expansion coefficients intermittently go through bifurcations in time where they cycle between having and not having secondary periodicities. The coefficients from modes $(10, 0)$, $(40, 0)$ and $(60, 0)$ exhibit behaviour which is indicative of two simple sinusoids while the other modes contain two periodicities with more complex behaviour.

For $1.55 < \alpha < 1.75$ all the modelled coefficients exhibit complex behaviour. The coefficients have oscillations with amplitude on the order of the initial conditions which then grow to larger amplitudes and eventually appear *chaotic*. The larger the value of α, the longer it takes the coefficients to exhibit large-amplitude behaviour. The large amplitudes observed are of $O(1)$ which is significantly greater than the initial conditions shown in table 1. This suggests two possibilities; (i) that α is too small and not able to remove enough energy from the system and (ii) there is too much production and some feedback would make sense. In § 7.6 we will see, by using the filter to lower production and include feedback, that the amplitudes of the modelled POD expansion coefficients more closely mimic the initial conditions.

https://doi.org/10.1017/S0022112001004803 Published online by Cambridge University Press

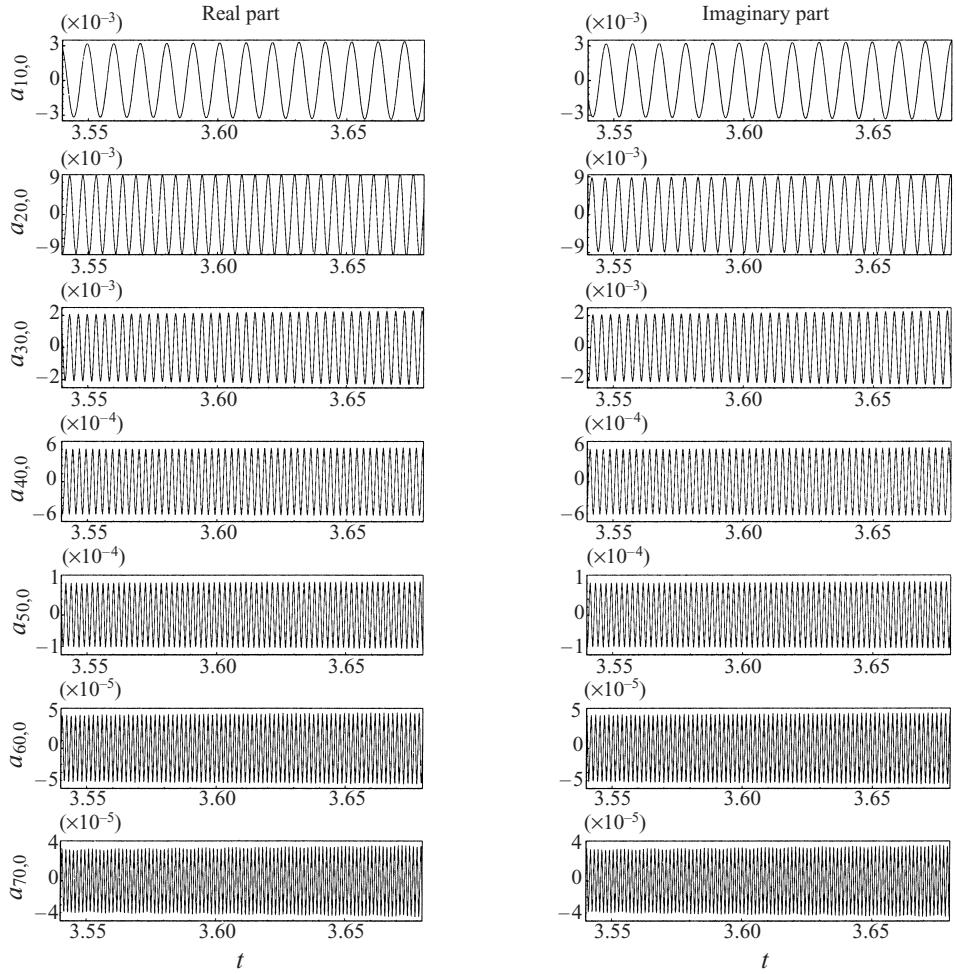


FIGURE 8. $a_{k_1,0}(t)$ time histories of real and imaginary parts of the modelled POD coefficients at $\alpha = 2.2$ for the seven-mode model.

7.3. *Reconstructed velocity field*

In this section, the modelled POD expansion coefficients from the seven-mode truncation are used with the POD eigenfunctions to reconstruct a low-dimensional instantaneous velocity field. This velocity is obtained by using the inverse Fourier transform of (2.4). For the $k_3 = 0$ simulations, u_3 is zero (recall from § 5.1 that $\Phi^{(1)}_{3,k_1,k_3=0} = 0$) and as a result, only reconstruction in the (x, y)-plane is possible.

Reconstruction from two values of α (2.2 and 1.85) are shown here. In the plots (figures 9 and 10), the flow goes from left to right and the time increment between snapshots is 4.0×10^{-04} s. This is five times the minimal resolved time step. The dimensions of the window are 345 mm in the x_1-direction and 66 mm in the x_2-direction. The figures are plotted in a frame of reference moving at the convection velocity U_c. Therefore, the velocity plotted is

$$u(x_2) + U(x_2) - U_c$$

where $U(x_2)$ is the mean streamwise velocity calculated for the particular truncation (see figure 7).

https://doi.org/10.1017/S0022112001004803 Published online by Cambridge University Press

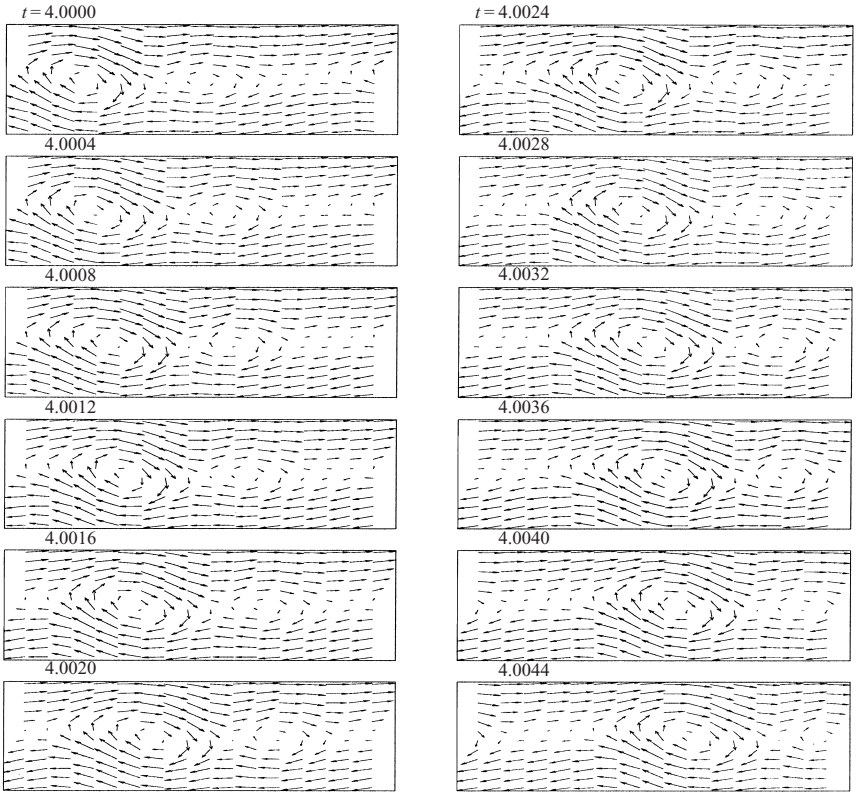


FIGURE 9. Velocity vector plots for $\alpha = 2.2$.

Figure 9 displays the velocity vector plots for $\alpha = 2.2$. The simulations yielded essentially periodic solutions. In the 'pseudo' real space plotted here, the periodicity is represented by what appear to be spanwise aligned vortices passing through the window. The structures pass through the window at evenly spaced intervals without interacting with each other. This type of solution is consistent with the results of Metcalfe *et al.* (1987) who observed roll-up without pairing in the absence of sub-harmonic excitation. These results are also similar to those of Rajaee *et al.* (1994) where the mixing layer was forced and periodic solutions with structures being convected through the resolved window were found. The average length of these structures, in the x_1-direction, is about 215 mm and in the x_2-direction they have a scale of order the vorticity thickness.

Figure 10 shows the velocity vector plots for $\alpha = 1.85$. This velocity field exhibits more active behaviour than that for $\alpha = 2.2$. Similar structures to those seen in the velocity field for $\alpha = 2.2$ can be observed passing through the windows along with other events. Note one major event observed in the first window ($t = 4$ s). This structure is much longer in the streamwise direction and appears to have two cores. This is how a pairing event would appear from a velocity vector plot, suggesting that even with such a simple model the initial signature of the pairing event is being captured. This organization however does not have the energy to wrap around as would be truly indicative of a pairing event and it appears that three-dimensional simulations are necessary to capture this type of behaviour.

https://doi.org/10.1017/S0022112001004803 Published online by Cambridge University Press

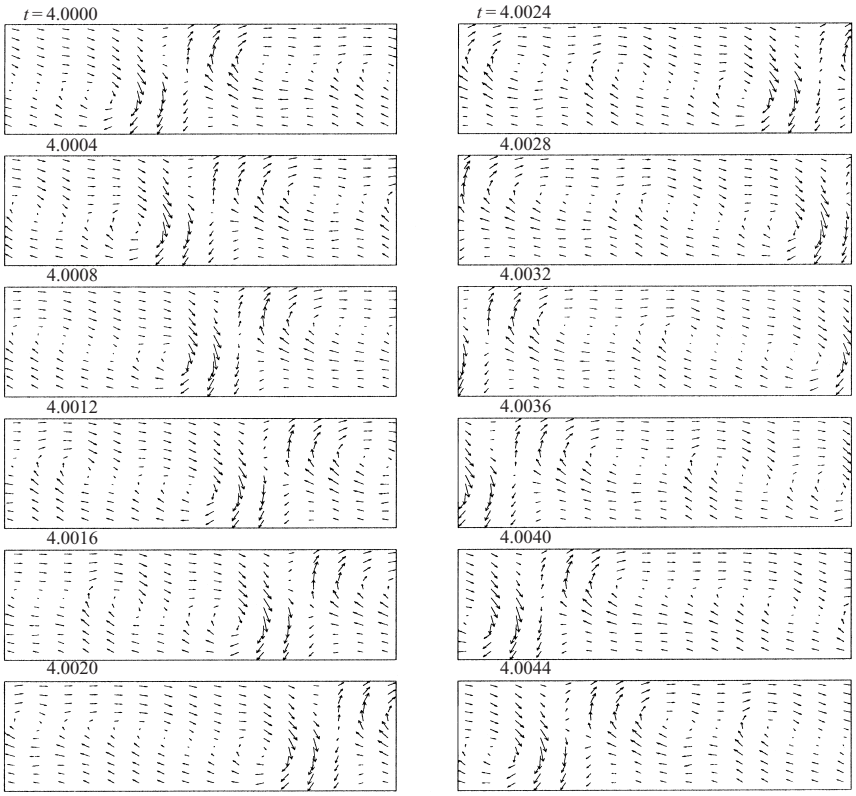


FIGURE 10. Velocity vector plots for $\alpha = 1.85$.

7.4. *Reconstructed energy profiles*

Once the velocity fields have been reconstructed, the kinetic energy profiles can also be reconstructed by averaging the time series data. These profiles can also be calculated directly from the first POD modes of the experimental data.

We will use the following equations to obtain the contribution of the first POD mode to the various components of the kinetic energy from both the modelled POD expansion coefficients and the experimental data:

$$\overline{u_i' u_j'}^{(1)}(x_2) = \int\int_{-\infty}^{+\infty} \Psi_{ij}^{(1)}(x_2; k_1, k_3)\, \mathrm{d}k_1 \mathrm{d}k_3 \tag{7.1a}$$

$$= \int\int_{-\infty}^{+\infty} \lambda_{k_1,k_3}^{(1)} \Phi_{i,k_1,k_3}^{(1)} \Phi_{j,k_1,k_3}^{(1)*}\, \mathrm{d}k_1 \mathrm{d}k_3. \tag{7.1b}$$

When the above integrals are performed using as input the experimental data they only contain contributions from the wavenumbers included in the model truncation (i.e. the filtered field). This allows an appropriate comparison between model and experiment.

Figure 11 is a plot of the various components of the turbulent kinetic energy profiles computed from measured data which only include contributions from the modes kept in the seven-mode model. The integral in wavenumber space is performed from $k_1 = 0$ to $70 \times \delta k_{1\,exp}$ for $k_3 = 0$. In this plot one can see that the kinetic energy from v is dominant. This is consistent with the discussion on the spectral tensor

https://doi.org/10.1017/S0022112001004803 Published online by Cambridge University Press

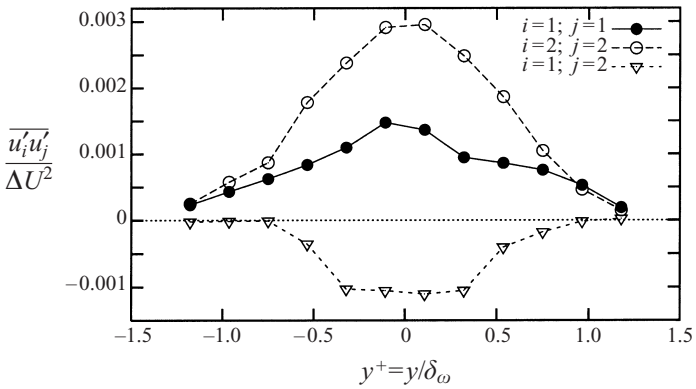


FIGURE 11. Turbulent kinetic energy profiles integrating from measured spectra for wavenumbers kept in the truncation.

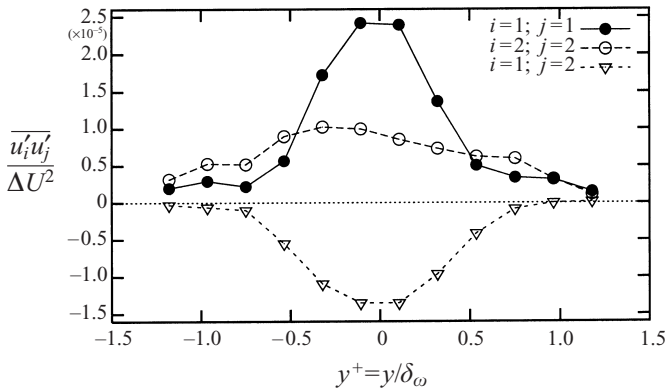


FIGURE 12. Turbulent kinetic energy profiles ($\alpha = 2.2$).

in Delville *et al.* (1999) where it was shown that the energy associated with v is dominant at $k_3 = 0$ while the energy associated with u is more broad band and spread out over several values of k_3. This figure shows a clear limitation of the seven-mode model and the modes kept. The filtered experimental field does not have the proper anisotropy given the severe truncation (especially the lack of non-zero spanwise wavenumbers).

Figures 12 to 14 are plots of the kinetic energy profiles for $\alpha = 2.2$, 1.85 and 1.7, respectively. All of these plots show the streamwise component of the Reynolds stress being dominant with an x_2-distribution similar to the filtered measured value (figure 11) but at substantially less amplitude (the closest in amplitude being the $\alpha = 1.75$ case). The modelled and filtered measured v-velocities show similar x_2-distributions. However, the v-component of the Reynolds stress from the model is substantially smaller in amplitude than the filtered measured results. It is so small that the filtered measured anisotropy (which is not correct) is totally different from that from the model. What is interesting is that the model results have an anisotropy similar to the unfiltered measured data (see figure 12, Delville *et al.* 1999). The model uv-profiles are similar in shape to the filtered measured values and have an amplitude approximately one-third of the streamwise kinetic energy profiles. This is also in good agreement with the unfiltered measured data of Delville *et al.* (1999).

https://doi.org/10.1017/S0022112001004803 Published online by Cambridge University Press

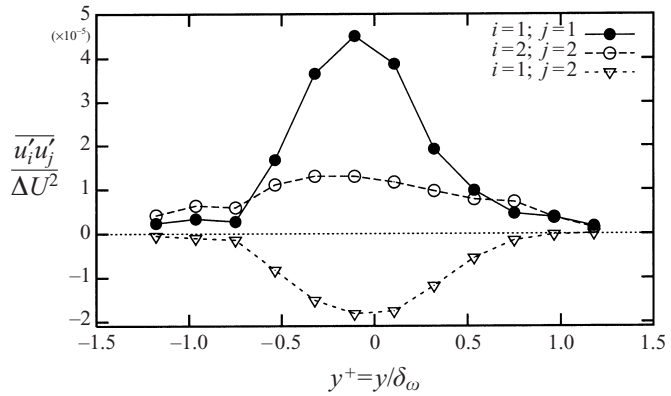


FIGURE 13. Turbulent kinetic energy profiles ($\alpha = 1.85$).

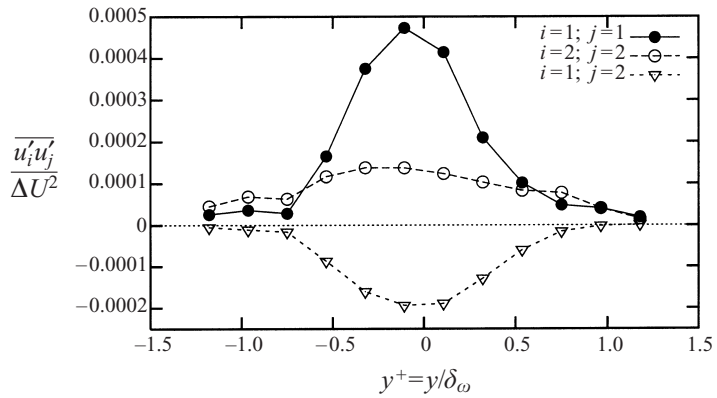


FIGURE 14. Turbulent kinetic energy profiles ($\alpha = 1.7$).

The swapping of dominance by the u-profile and the v-profile between the model and filtered measured results occurs because the POD expansion coefficients for the first two modes from the simulations, $a_{10,0}$ and $a_{20,0}$, are dominant in amplitude. As was discussed earlier, this is the wrong distribution when compared to the initial conditions. It was shown in the discussion of the spectra in Delville *et al.* (1999) that streamwise wavenumbers less than $5.8\,\mathrm{m}^{-1}$ are associated with u-energy at the centre of the mixing layer. When calculating the profiles in figures 12 to 14 the two first modes become the dominant terms in the integration over streamwise wavenumber, thus making the u-energy profile dominant. The improper (when compared to initial conditions) energy distribution of the model results in an anisotropy consistent with the unfiltered experimental data. These results clearly indicate there are inconsistencies between the model and filtered experiments. This suggests that including non-zero spanwise wavenumbers in the models for the POD expansion coefficients is critical for capturing both the proper initial conditions and the proper anisotropy.

7.5. *Spectra of reconstructed velocity*

Figures 15 and 16 display autospectra, calculated from the reconstructed velocities discussed above, for the u-component and the v-component of velocity, respectively. In these plots the y-axis has units of $\mathrm{m}^2\,\mathrm{s}^2\,\mathrm{Hz}^{-1}$ while the x-axis is frequency. Only the spectra from half of the mixing layer are included here because the upper and lower

https://doi.org/10.1017/S0022112001004803 Published online by Cambridge University Press

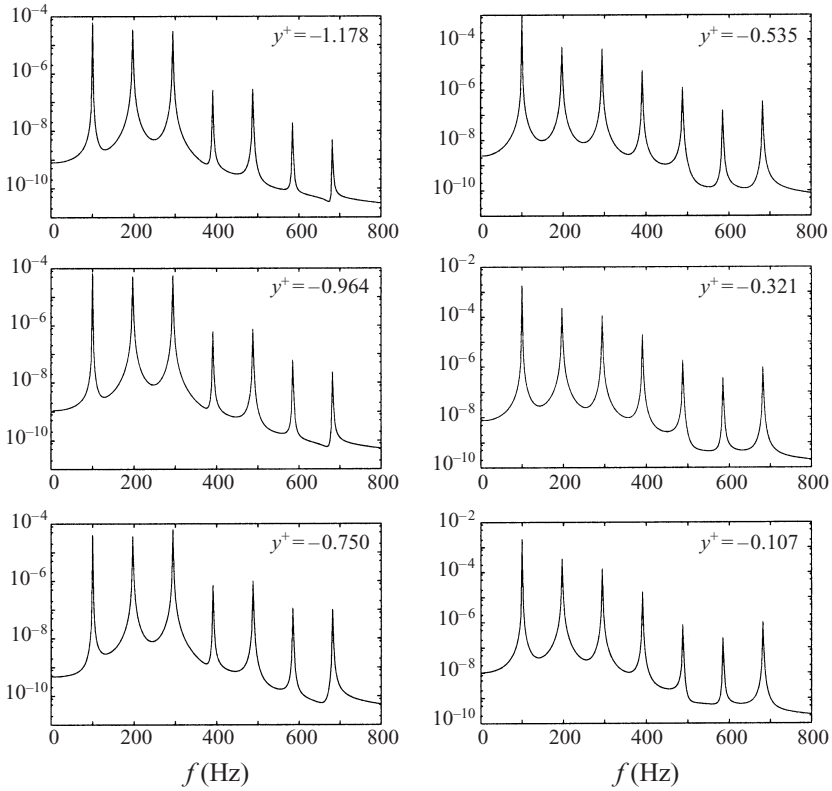


FIGURE 15. Autospectra of u_1-component for $\alpha = 1.85$.

halves demonstrated the same characteristics consistent with the measured spectra presented in Delville *et al.* (1999). Only spectra for $\alpha = 1.85$ are shown because the behaviour described below is representative of results for α around this range.

In figure 15, the x_2-distribution of energy that was discussed in the experimental work on spectra (see Delville *et al.* 1999) is seen here as well. For the outer part of the mixing layer, $x_2/\delta_\omega = -0.75$ to -1.178, the energy distribution is similar to that for the v-component and contains information near the dominant Strouhal number. In the centre of the mixing layer, the energy is contained at lower frequencies.

For the v-component of velocity (figure 16), a similar energy distribution in frequency is obtained regardless of the x_2-location but, as expected, the amplitudes reach a maximum near the centre of the mixing layer. The frequencies observed from the model correspond closely to the experimentally observed values.

In summary, the behaviour described here for the x_2-distribution of the spectra mimics well the experimental behaviour presented in Delville *et al.* (1999). Even with the problems of the model discussed earlier (improper wavenumber distributions and anisotropy) it is very encouraging that our severely truncated model has the correct temporal trends as seen in the frequency spectra.

7.6. *Seven-mode model with feedback via filter*

The results of the seven-mode model without feedback for very small α indicate that there is a need to control the production and provide for feedback between the mean flow and the modelled coefficients. In this section, the solution of (4.1), written for

https://doi.org/10.1017/S0022112001004803 Published online by Cambridge University Press

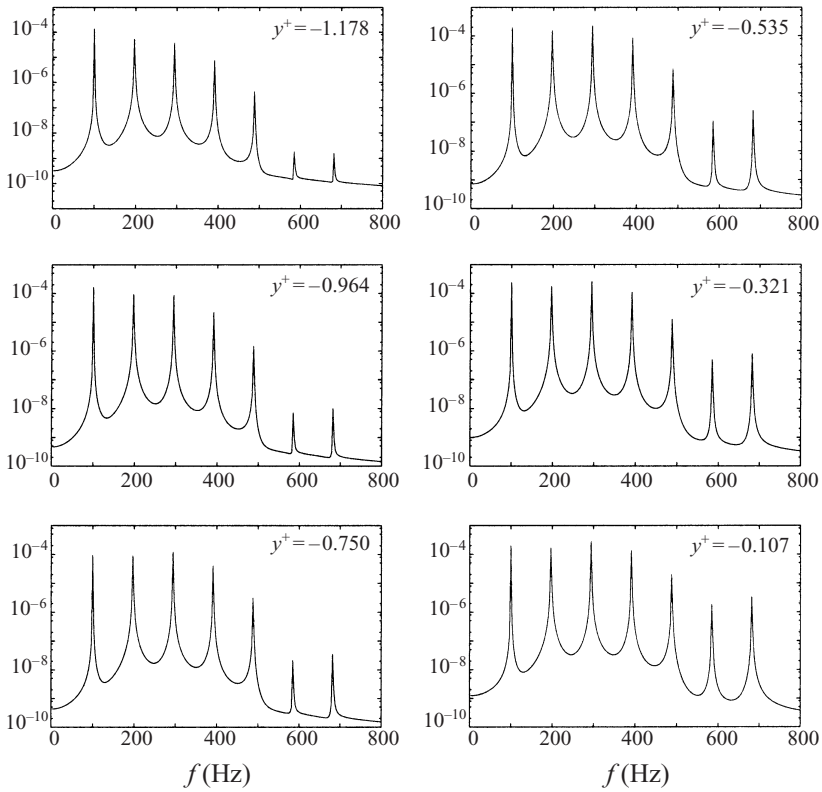


FIGURE 16. Autospectra of u_2-component for $\alpha = 1.85$.

the filter case, will be discussed for the seven-mode system retained in § 7.1. With the method of closure of (3.6), the mean velocity is split into a steady part that is held constant for all time and a time-dependent part that manifests itself as a cubic term in the dynamical equations. The introduction of this filtering technique discussed in § 3 allows time-dependent interaction between the coherent structures and mean velocities. This technique will also allow the scaling of the production term. The need for this will become even more apparent when truncations involving $k_3 \neq 0$ are discussed in § 8.

Figure 17 shows U_{1F} estimated from (3.5) for different values of k_{1C} and k_{3C}. For values of $k_{1C} = 50$ or 60, the mean velocity profiles are essentially the same as the one used in the no-feedback case ($k_{1C} = 70$ and $k_{3C} = 0$ in figure 17). As one should expect, the lower the value of k_{1C}, the smaller the mean velocity gradient.

7.6.1. *Filter cutoff* = (50, 0) *or* (40, 0)

Since the simulations of the no-feedback model yielded reasonable results except at very small values of α, a natural first step was to set $k_{1C} = 50$. This allows some contribution to the cubic term without much loss in mean streamwise velocity gradient. Upon further examination of figure 17, it is clear that the profiles obtained for U_{1F} using $k_{1C} = 40$ or $k_{1C} = 50$ are very similar, and in fact when these two values of k_{1C} were used to calculate the mean profile similar dynamics were found for the modelled POD expansion coefficients. Since the filtered mean streamwise velocity profile is similar in this case to the unfiltered one, the production terms in (4.1) are

https://doi.org/10.1017/S0022112001004803 Published online by Cambridge University Press

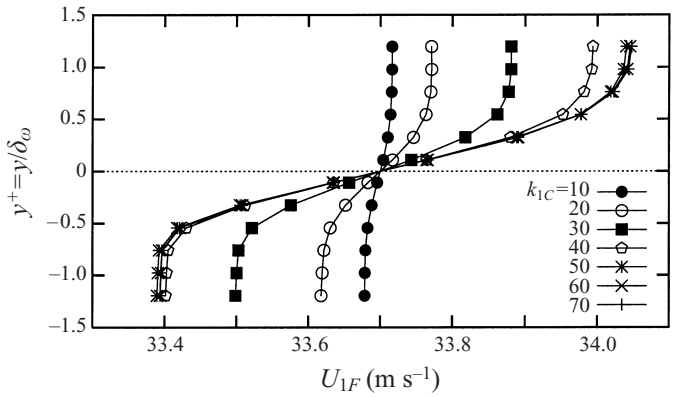


FIGURE 17. Mean streamwise velocity profiles for different filter values; $k_{3C} = 0$.

of the same order of magnitude. In this case however the introduction of the cubic term provides feedback between the modelled coefficients and the mean streamwise velocity.

Initial results from the numerical simulations showed that the introduction of the cubic term had a stabilizing effect on the system†. For values of $\alpha > 1.55$ the behaviour is the same as for the no-feedback case and is still characterized by the descriptions in table 3. With feedback, however, for values of $\alpha < 1.55$ the system no longer exhibits the unbounded growth mentioned in the discussion of the no-feedback case. For values of α in this range the system now exhibits a complex behaviour in full space on top of the underlying periodicities, much the same as in the region $1.8 > \alpha > 1.55$ for the no-feedback case. For example, when $\alpha = 0.5$, the complex behaviour is similar to that of the no-feedback simulations although the mean-square amplitudes of the coefficients have increased even more. These characteristics were observed whether $k_{1C} = 50$ or $k_{1C} = 40$.

7.6.2. *Other values for cutoff wavenumber*

For values of k_{1C} smaller than 40, the system took on different characteristics, which indicates the importance of having the correct level of production. Comparative results for the solutions with $k_{1C} = 20$ and $k_{1C} = 30$ exhibit similar dynamical behaviour. The systems yielded trivial solutions except for very small values of α. For these small values, the dynamics were very similar to the complex behaviour discussed for the no-feedback model although the mean-square amplitudes of the coefficients were more reasonable when compared to the experimental values. As one would expect for k_{1C} less than 20, the system more closely mimics the limiting case examined in § 6. As the production term becomes smaller and smaller, the solutions decay to zero. The reason for this is again the lack of linear growth as discussed in § 6.

8. Truncations for $k_3 \neq 0$

The modelled POD expansion coefficients obtained from the $k_3 = 0$ simulations give temporal and spectral distributions which are reasonable but are unable to capture the proper spatial wavenumber spectral distributions and velocity component

† Recall that in the context of dynamical system theory, the cubic terms may have stabilizing effects when their contribution is the opposite of the linear term contribution.

https://doi.org/10.1017/S0022112001004803 Published online by Cambridge University Press

https://doi.org/10.1017/S0022112001004803 Published online by Cambridge University Press

(k_1, k_3)	(10, 0)	(20, 0)	(30, 0)	(40, 0)	(50, 0)	
$a_{k_1,k_3}(t=0)$	$7.60000\,10^{-03}$	$1.13771\,10^{-02}$	$1.72755\,10^{-02}$	$2.06431\,10^{-02}$	$1.72524\,10^{-02}$	
(k_1, k_3)	(0, 1)	(10, 1)	(20, 1)	(30, 1)	(40, 1)	(50, 1)
$a_{k_1,k_3}(t=0)$	$6.80040\,10^{-03}$	$7.53926\,10^{-03}$	$1.20971\,10^{-02}$	$1.96608\,10^{-02}$	$2.42085\,10^{-02}$	$2.07484\,10^{-02}$
(k_1, k_3)	(0, 2)	(10, 2)	(20, 2)	(30, 2)	(40, 2)	(50, 2)
$a_{k_1,k_3}(t=0)$	$7.10371\,10^{-03}$	$7.09660\,10^{-03}$	$9.41142\,10^{-03}$	$1.26013\,10^{-02}$	$1.43849\,10^{-02}$	$1.18079\,10^{-02}$
(k_1, k_3)	(0, 3)	(10, 3)	(20, 3)	(30, 3)	(40, 3)	(50, 3)
$a_{k_1,k_3}(t=0)$	$6.74773\,10^{-03}$	$6.58099\,10^{-03}$	$8.20589\,10^{-03}$	$9.57029\,10^{-03}$	$1.02790\,10^{-02}$	$8.29034\,10^{-03}$

TABLE 4. Wavenumber pairs and initial conditions for the 38-mode model.

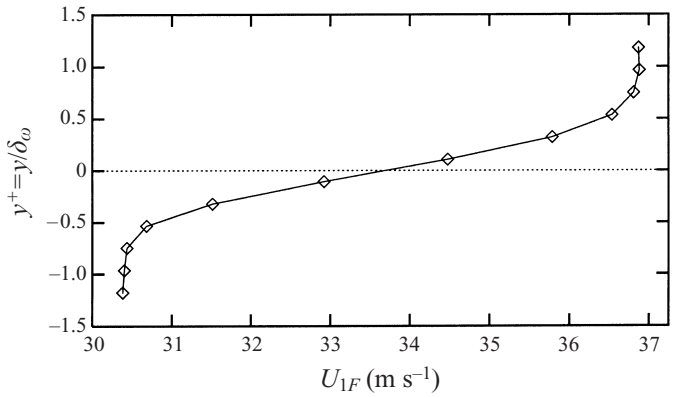


FIGURE 18. Mean streamwise velocity profiles for 38-mode model, no-feedback case.

anisotropies. In an attempt to try and capture more realistic behaviour for the latter two, simulations of the modelled POD expansion coefficients, which include non-zero spanwise wavenumbers, were performed. Results from a 38-mode model are described in this section both with and without filtered equations (i.e. both with and without feedback).

The specific truncation studied here is an extension of a five-mode model ($k_1 = 10, 20, 30, 40, 50; k_3 = 0$) discussed in Ukeiley (1995). This system exhibited essentially the same dynamics as the seven-mode system described in § 7. Here we use the five-mode system because it allows inclusion of non-zero spanwise wavenumbers without the system becoming too large. Non-zero spanwise wavenumbers added to the five-mode system include $k_3 = 1,\ 2$ and 3. The wavenumber pairs and initial conditions used for the 38-mode simulations are tabulated in table 4.

8.1. *No-feedback relationship*

Figure 18 displays the no-feedback mean profile used for the simulations discussed in this section. It has a larger gradient than those used for the $k_3 = 0$ simulations, as can be seen by comparing with the mean profiles shown in figure 17. This provides more production resulting in additional energy for the system.

8.1.1. *Dynamics as a function of α, no feedback*

In the next section we present time series for the case with feedback at one value of α. Here we only summarize the results for the no-feedback model. The results from the simulations including some feedback are more realistic as will be discussed later. Table 5 summarizes the dynamics of the system of equations as a function of α for the 38-mode model with no feedback. The values of α where interesting dynamics occur are much higher than with the seven-mode model. However, with the 38-mode model, the same underlying frequencies, as a function of k_1 (see table 2), were observed regardless of the value of k_3. This model now includes three modes involving $k_1 = 0$. For these $k_1 = 0$ modes there is no underlying frequency and the solutions are more intermittent than periodic. As with the seven-mode no-feedback simulations there is a value for α below which the solutions to the equations grow unbounded. For the 38-mode simulations this value was $\alpha = 36.5$. With α greater than 65 the viscous dissipation term is dominant, and a trivial solution is the global attractor.

When $36.5 > \alpha > 39$, the system switched between complex behaviour and unbounded growth with small changes in α. When the solutions did not grow unbounded,

https://doi.org/10.1017/S0022112001004803 Published online by Cambridge University Press

Value of α	Behaviour
$\alpha < 36.5$	All modes grow unbounded to infinity
$36.5 < \alpha < 39$	Unstable solutions switching between unbounded growth and complex behaviour with low-order amplitude coefficients
$39 < \alpha < 45.5$	Complex behaviour in full space
$45.5 < \alpha < 47$	Complex behaviour for $k_3 = 0$ Intermittent behaviour for $k_3 \neq 0$
$47 < \alpha < 52.6$	System blows up
$52.6 < \alpha < 57$	Complex behaviour for $k_3 = 0$ Trivial solution for $k_3 \neq 0$
$57 < \alpha < 65$	Intermittent/periodic solution $k_3 = 0$ Trivial solution for $k_3 \neq 0$
$\alpha > 65$	Trivial solution for all space

TABLE 5. Description of dynamics for the 38-mode no-feedback model.

all the modes exhibited a complex 'random' solution over the underlying periodicity. The behaviour of the system for α between 39 and 45.5 is similar to the bounded results for $36.5 > \alpha > 39$. The solutions for the $k_3 = 0$ POD expansion coefficients exhibit very similar dynamics to one another. However, the solutions for $k_3 \neq 0$ switch between behaviour similar to that for $k_3 = 0$ and an intermittent type of behaviour with the amplitude of the coefficients going to zero between events. As α approaches 47 the amplitude of the coefficients for $k_3 = 0$ grows until in the region of α between 47 and 52.6 they drive the system unstable.

The dynamics for α between 52.6 and 65 follow trends similar to the seven-mode model for α between 2.05 and 2.45, especially in the observed intermittent behaviour. For all the modes with $k_3 \neq 0$, a trivial solution was obtained, while for $k_3 = 0$, all modes in k_1 exhibited active dynamics. These modes evolved through periodic solutions with the underlying periodicity remaining constant and the secondary periods becoming larger and larger. As with the seven-mode simulations, mode $(20, 0)$ is controlling the dynamical behaviour of the system. This mode grows in amplitude and triggers mode $(40, 0)$. These two modes distribute their energy to the rest of the system. At these values of α, the system is being damped so much that no variations in the streamwise direction can arise. However, this is the only range of α that has realistic amplitudes for the modelled POD coefficients. At the lower values of α where the solutions show three-dimensional behaviour the mean-square amplitudes of the modelled coefficients are much too large. This suggests that in the no-feedback case too much production is being provided for the system and that some feedback is necessary to obtain coefficient amplitudes of the right order while retaining three-dimensional dynamics.

8.1.2. *Representation in physical space, no-feedback*

Figures 19 and 20 display the individual components of the turbulent kinetic energy profiles for $\alpha = 39$ and 45, respectively. As with the seven-mode dynamical system, these systems exhibit distributions in the x_2-direction similar to the experimental distributions. For both cases the streamwise component of the turbulent kinetic energy is much higher than expected. For $\alpha = 45$ the reconstructions of the streamwise component of the turbulent kinetic energy from the simulations are even greater than the first POD mode reconstructed experimental values which include contributions

https://doi.org/10.1017/S0022112001004803 Published online by Cambridge University Press

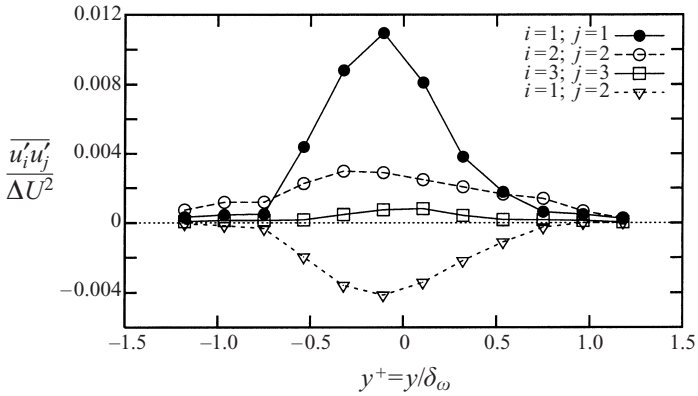


FIGURE 19. Turbulent kinetic energy profiles for $\alpha = 39$ (38-mode model).

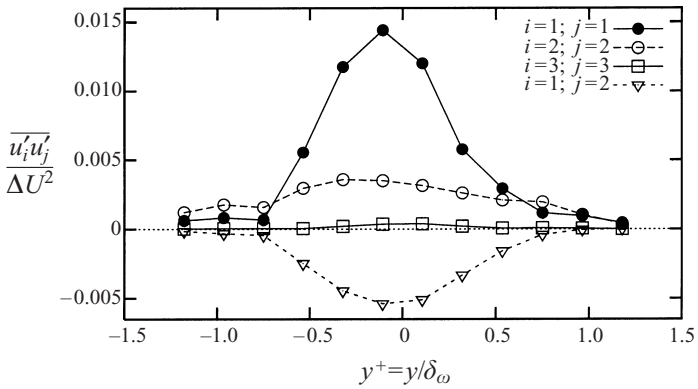


FIGURE 20. Turbulent kinetic energy profiles for $\alpha = 45$ (38-mode model).

from all wavenumbers, not just those used in the simulations. The amplitude of the Reynolds stress were always found to be significantly larger than those of the filtered experimental values as well.

These unrealisticly high amplitudes are a direct result of the high amplitudes of the modelled POD expansion coefficients. The mean streamwise velocity profile shown in figure 18 causes too much production and the system cannot obtain a three-dimensional solution with realistic values for the coefficients. This shows why there is a need to scale the linear growth term and provide some feedback.

8.2. *38-mode model filter relationship*

The results discussed for the 38-mode no-feedback model suggest that using the filter technique would prove useful in scaling the production term and obtaining coefficients with a more realistic amplitude. Several values of filter setting (k_{1C};k_{3C}) have been evaluated in this study. For values of the filter that drasticly reduced the mean streamwise velocity gradient, the system exhibited a behaviour where the coefficients were always decreasing (for example in Ukeiley 1995 simulations were presented where all of the mean velocity was modelled in the feedback term). For values where the filter did not alter the mean streamwise velocity gradient significantly, the system behaved similarly to the no-feedback results discussed in the previous section, as was expected. Finally, a setting of $k_{1C} = 40$ and $k_{3C} = 2$ was selected because at this

https://doi.org/10.1017/S0022112001004803 Published online by Cambridge University Press

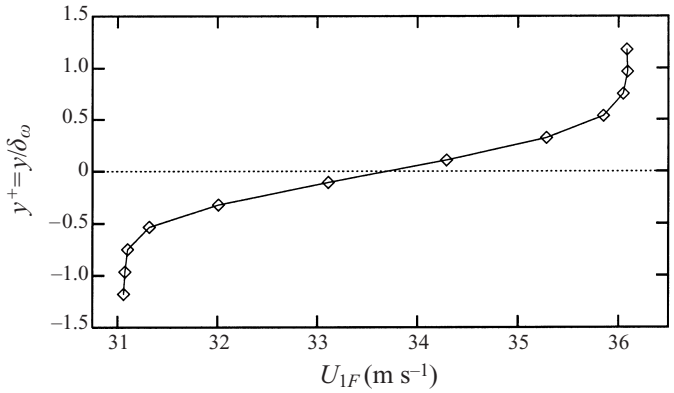


FIGURE 21. Mean streamwise velocity profiles for filter setting of (40, 2) (38-mode model).

setting the proper amplitude for the modelled POD expansion coefficients along with three-dimensional solutions were obtained.

8.2.1. *Filter cutoff* (40, 2)

Figure 21 shows a profile of U_{1F} calculated with a filter setting of (40, 2). It has a noticeably smaller gradient than that of the unfiltered case (compare with figure 18) resulting in a reduction of the production term in (4.1). The smaller production term should limit the energy input to the model resulting in coefficients with smaller amplitudes.

The dynamics exhibited as a function of α are simpler than for the no-feedback case described in the previous section. For $\alpha < 35$ the system is unstable and the solutions grow to infinity. For values of $\alpha > 39$ the system has the same basic behaviour as in the 38-mode no-feedback simulations. There is however a range, $39 > \alpha > 35$, where the system has active dynamics for all modes (i.e. three-dimensional) with realistic POD coefficient amplitudes. Hence we focus our attention on the modelled POD expansion coefficients obtained within this range of α.

Figure 22 displays the time traces for $\alpha = 36.65$. Only time histories of the coefficients for positive values of k_1 are shown since the values for negative k_1 exhibited similar dynamics to their positive counterparts. In this figure, all modes exhibit the underlying periodicities, with a more complex second periodic behaviour sitting on top.

Figure 23 displays the turbulent kinetic energy profiles for $\alpha = 36.65$. The behaviour in the x_2-direction is the same as has been observed in the no-feedback case; however the amplitudes are significantly smaller, being now of the same order as those obtained from integrating the measured spectra over the first POD mode contribution from the wavenumbers kept in the model. The ratio of the mean-square u_1-component to the mean-square u_2-component is now comparable to original experimental values shown in Delville *et al.* (1999). It should be pointed that with the inclusion of non-zero spanwise wavenumbers, integrating the experimental spectra over the model domain yielded anisotropy ratios close to the measured experimental values.

Figures 24 and 25 plot the u_1- and u_2-autospectra for the case discussed above. The axes on these plots have the same units as for figures 15 and 16. The u_3-component is not shown because its magnitude was quite small as demonstrated by the amplitude of the u_3-component of the turbulent kinetic energy shown in figure 23. As with the

https://doi.org/10.1017/S0022112001004803 Published online by Cambridge University Press

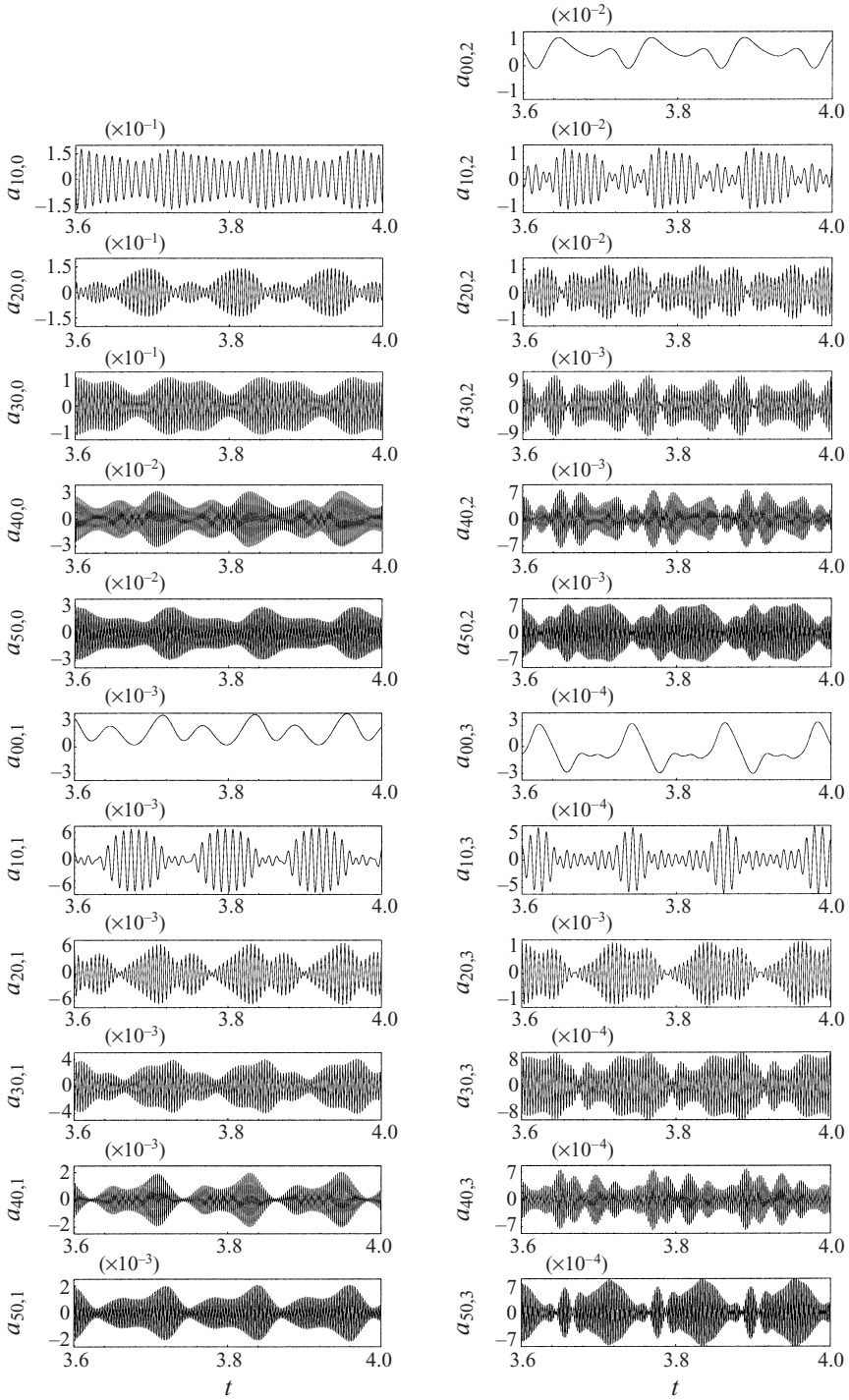


FIGURE 22. Real part of $a_{k_1,k_3}(t)$ $\alpha = 36.65$ for a filter setting of (40, 2) (38-mode system), short time evolution. For clarity, each plot is labelled only with the value of (k_1, k_3).

https://doi.org/10.1017/S0022112001004803 Published online by Cambridge University Press

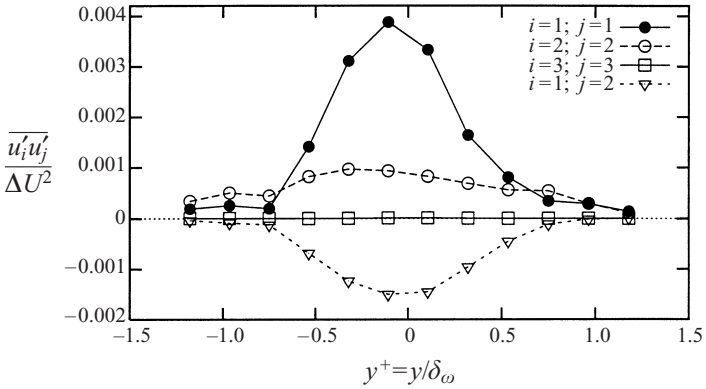


FIGURE 23. Turbulent kinetic energy profiles for $\alpha = 36.65$ with a cutoff filter of (40, 2) (38-mode model).

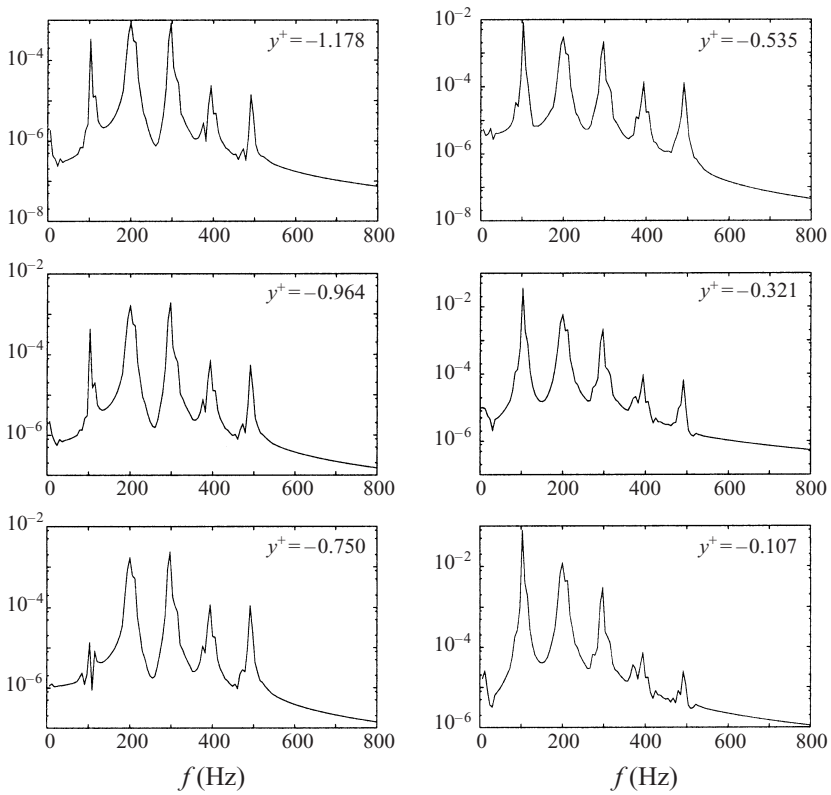


FIGURE 24. Autospectra of u_1-component for $\alpha = 36.65$.

seven-mode system (§ 7.5), only values from the bottom half of the mixing layer are shown due to the symmetric nature of the flow.

The frequency content of the u_2-component does not change as a function of the x_2-location, and the amplitude of the spectral peaks gets larger near the centre of the mixing layer. The u_1-component has a shift in the frequency between the inner and outer parts of the mixing layer: the outer region has the same frequency content as the u_2-component and the inner part has a dominant frequency of approximately one-half the

https://doi.org/10.1017/S0022112001004803 Published online by Cambridge University Press

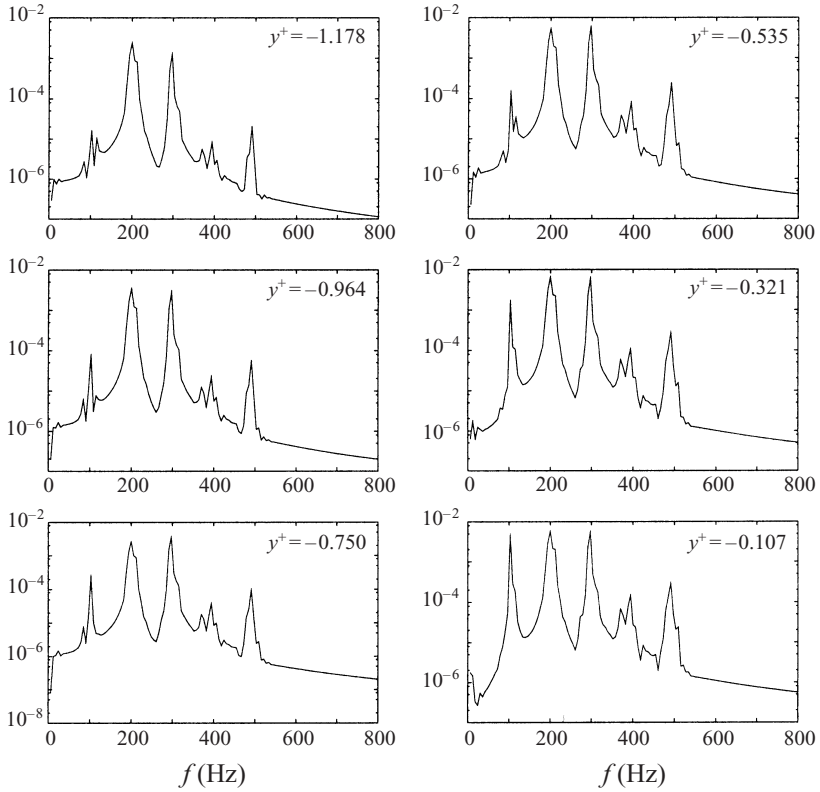


FIGURE 25. Autospectra of u_2-component for $\alpha = 36.65$.

outer. The spectral peaks are now noticeably broader than those shown in figures 15 and 16 because more modes have been included in the system, each with its own spectral content. These results are qualitatively similar to the measured spectra as shown in Delville *et al.* (1999) and to the seven-mode system simulations described earlier.

Figures 26 and 27 show plots, at $t = 3.6$ s, of the total vorticity ($|\omega_1|+|\omega_2|+|\omega_3|$) for the (x_1, x_2)- and (x_2, x_3)-planes, respectively. In figure 26, a slice of the flow at $x_3 = 0$ is displayed: several spanwise vortices can be seen, e.g. the two contour peaks at locations B and F along with the two in the other half of the domain. Figure 27 displays the (x_2, x_3)-plane contours of the vorticity at the locations marked on figure 26, and shows clear evidence of streamwise aligned vortices in x_1 between the two spanwise vortices. These are represented by the contour lines at locations D and E which lie between the spanwise vortex centres at locations B and F. This result is in good agreement with previous studies of the mixing layer (Metcalfe *et al.* 1987), which show strong evidence that spanwise vortex tubes are connected by streamwise aligned vorticity. The average ratio of the spanwise distance between structures to that of the streamwise structures is approximately 0.7 for the simulations presented here. This is in good agreement with the results of Pierrehumbert & Widnall (1982) where the most unstable spanwise wavelength was shown to be approximately 2/3 of the streamwise wavelength.

9. Conclusions

In this work, a low-order dynamical system model has been presented which is valid for the asymptotic region of a plane turbulent mixing layer. The ordinary differential

https://doi.org/10.1017/S0022112001004803 Published online by Cambridge University Press

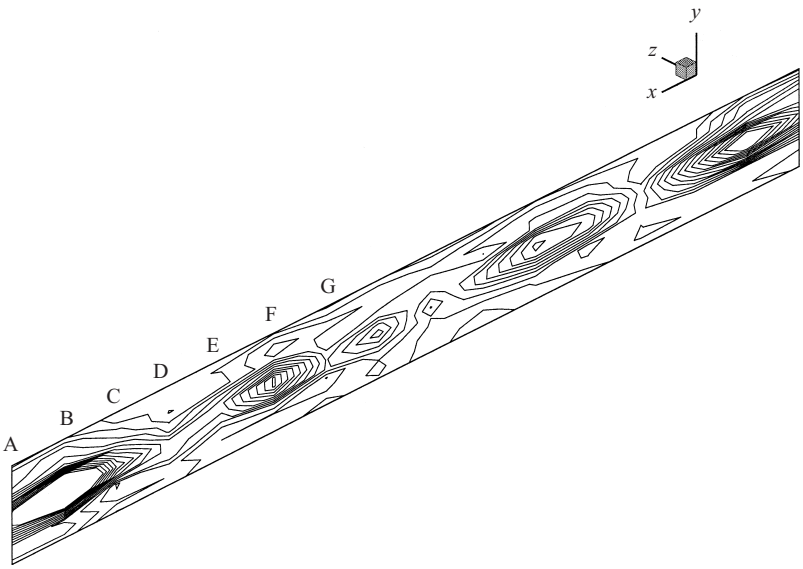


FIGURE 26. Vorticity $\alpha = 36.65$ for a filter setting of (40, 2) (38-mode system), (x_1, x_2)-plane.

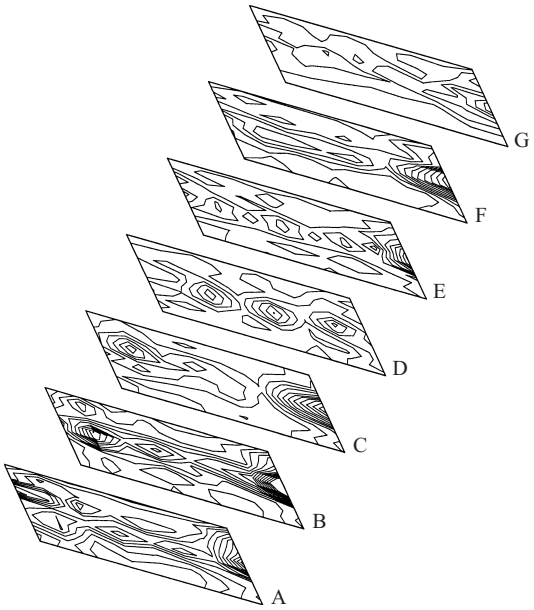


FIGURE 27. Vorticity $\alpha = 36.65$ for a filter setting of (40, 2) (38-mode system), (x_2, x_3)-plane.

equations of the reduced-order model are derived from a Galerkin projection of the Navier–Stokes equations and the POD eigenfunctions reported in Delville *et al.* (1999). The low-dimensional nature of the model is achieved by only keeping equations for selected streamwise/spanwise wavenumbers and the first POD mode. Specifically, two sets of equations, each with a different means of representing the mean streamwise velocity, have been presented for two different truncations. In the first mean closure, termed no feedback, a Boussinesq approximation was used to calculate the contribution from the modes kept in the truncation to the mean

https://doi.org/10.1017/S0022112001004803 Published online by Cambridge University Press

streamwise velocity. The mean velocity profile was then held constant for all time causing a fixed level of production. The other set of equations that was studied, termed feedback, allowed both linear growth and feedback between the turbulence and the mean. In this method, a cutoff wavenumber was chosen and wavenumbers greater than this value were allowed to vary with time while the contribution from wavenumbers less than this value contribute in a non-time-dependent manner as with the first set of equations.

The first truncation involved seven modes evenly spaced in k_1 for $k_3 = 0$. Regardless of the value of the bifurcation parameter this system always exhibited an underlying periodicity with the streamwise wavenumbers kept in the truncation. The underlying periodicity, although sometimes embedded in a more complex behaviour, is representative of the spanwise vortex tubes which are known to be a periodic event. Reconstructions of the instantaneous velocity field showed further evidence that the seven-mode model represented the periodic spanwise vortex organization well. Examination of the turbulent energy profiles showed that the anisotropy matched that of the experiment, not that of the small set of modes kept in the model. The second mean closure, i.e. the filter technique, was found to have a stabilizing effect on the simulations. For filter settings which did not significantly alter the mean streamwise velocity gradient the introduction of the cubic term served to stabilize the solutions. The system did not go unstable and exhibit unbounded growth regardless of the value of α.

A truncation which involved spanwise wavenumbers not equal to zero was also examined. Simulations for this truncation using the no-feedback mean closure overpredicted the kinetic energy profiles due to the production term being to large. Applying the filter technique had a pronounced effect by scaling of the mean streamwise velocity gradient. This in turn reduced the production term thus resulting in magnitudes for the coefficients that were in good agreement with the experimentally determined ones. With the reduced energy in the system the amplitudes of the reconstructed mean-square velocity profiles were consistent with what one would expect from the severely truncated system. Plots of the total vorticity showed strong evidence of the known flow organizations. These plots showed spanwise vortex tubes being connected by streamwise aligned vorticity. This type of structure is consistent with what has been reported in many previous studies (see Metcalfe *et al.* 1987 for example). The fact that the system exhibits the correct essential physics makes it a likely candidate in developing control strategies for the mixing layer such as those proposed for the dynamical systems model of the near-wall region by Berkooz (1992).

This work was completed with the support of the French Ministry of Defense under the Grants DRET/DGA 90-171 and DRET/DGA 93.2549.A and a NSF/CNRS travel grant through the international program. Partial support for L.U. was provided by the French Ministry of Foreign Office under the Chateaubriand program. The authors would like to acknowledge the constructive comments of the referee.

Appendix A. General dynamical equations

A.1. *No-feedback relationship*

$$\Lambda^{1(m)}_{k_1,k_3} = \nu \left[-4\pi^2(k_1^2 + k_3^2)\delta_{mn} + \int_{-L_2}^{L_2} \left(\frac{\mathrm{d}^2 \Phi^{(m)}_{i,k_1,k_3}(x_2)}{\mathrm{d}x_2^2} \right) \Phi^{(n)*}_{i,k_1,k_3}(x_2)\, \mathrm{d}x_2 \right]. \qquad \text{(A 1)}$$

https://doi.org/10.1017/S0022112001004803 Published online by Cambridge University Press

$$\Lambda^{2(m)}_{k_1,k_3} = -\left(\int_{-L_2}^{L_2} \Phi^{(m)}_{2,k_1,k_3}(x_2')\frac{\partial U_1(x_2')}{\partial x_2}\Phi^{(n)*}_{1,k_1,k_3}(x_2')\,\mathrm{d}x_2' + (2\pi \mathrm{i}k_1)\int_{-L_2}^{L_2} U_1(x_2')\Phi^{(m)}_{i,k_1,k_3}(x_2')\Phi^{(n)*}_{i,k_1,k_3}(x_2')\,\mathrm{d}x_2'\right). \tag{A 2}$$

$$Q^{(p)(q)}_{k_1',k_3',k_1,k_3} = -\frac{(1-\delta_{k_1,0}\delta_{k_3,0})}{(L_1L_3)^{1/2}} \times \int_{-L_2}^{L_2}\Big[2\pi \mathrm{i}(k_1-k_1')\Phi^{(p)}_{1,k_1',k_3'}(x_2)\Phi^{(q)}_{i,k_1-k_1',k_3-k_3'}(x_2) + \Phi^{(p)}_{2,k_1',k_3'}(x_2)\frac{\mathrm{d}}{\mathrm{d}x_2}\Phi^{(q)}_{i,k_1-k_1',k_3-k_3'}(x_2) + 2\pi \mathrm{i}(k_3-k_3')\Phi^{(p)}_{3,k_1',k_3'}(x_2)\Phi^{(q)}_{i,k_1-k_1',k_3-k_3'}(x_2)\Big]\Phi^{(n)*}_{i,k_1,k_3}(x_2)\,\mathrm{d}x_2. \tag{A 3}$$

A.2. *Filter relationship*

$$C^{(p)(q)(r)}_{k_1',k_3',k_1,k_3} = \frac{1}{v_e(L_1L_3)}\left[\int_{-L_2}^{L_2}\left[\left(\int_0^{x_2}\Phi^{(p)}_{1,k_1',k_3'}(x_2')\Phi^{(q)*}_{2,k_1',k_3'}(x_2')\,\mathrm{d}x_2'\right)(2\pi \mathrm{i}k_1)\Phi^{(r)}_{i,k_1,k_3}(x_2) + \delta_{i1}\left(\Phi^{(p)}_{1,k_1',k_3'}(x_2)\Phi^{(q)*}_{2,k_1',k_3'}(x_2)\Phi^{(r)}_{2,k_1,k_3}(x_2)\right)\right]\Phi^{(n)*}_{i,k_1,k_3}(x_2)\,\mathrm{d}x_2\right]. \tag{A 4}$$

Appendix B. Turbulent viscosity model

In Aubry *et al.* (1988) the assumption that small scales remove energy from larger ones is written in the following form:

$$\tau^{SS}_{ij} = -2\nu_T S^{LS}_{ij}, \tag{B 1}$$

denoting that the small-scale stress tensor is proportional to the strain rate tensor for the modes resolved. In this equation, τ^{SS}_{ij} and S^{LS}_{ij} are defined as

$$\tau^{SS}_{ij} = \overline{\overline{u_i}^{SS}\overline{u_j}^{SS}}^{SS} - \overline{\overline{u_i}^{SS}\overline{u_j}^{SS}}^{SS} - \tfrac{1}{3}\delta_{ij}\left(\overline{\overline{u_k}^{SS}\overline{u_k}^{SS}}^{SS} - \overline{\overline{u_k}^{SS}\overline{u_k}^{SS}}^{SS}\right), \tag{B 2}$$

and

$$S^{LS}_{ij} = \frac{1}{2}\left(\frac{\partial \overline{u_i}^{LS}}{\partial x_j} + \frac{\partial \overline{u_j}^{LS}}{\partial x_i}\right), \tag{B 3}$$

where the notation $\overline{()}^{LS}$ (large scale) corresponds to the summation over all the modes and wavenumbers inferior or equal to the truncation point; the notation $\overline{()}^{SS}$ corresponds to the small scales (summation over all the mode wavenumbers larger than the truncation point). By observing that the energy decreases rapidly with higher POD and streamwise/spanwise wavenumber modes (see the three-dimensional eigenspectra represented in Delville *et al.* 1999), the assumption can be made that the relevant scales are given by characteristic scales of the first neglected modes.

https://doi.org/10.1017/S0022112001004803 Published online by Cambridge University Press

With these conditions the turbulent viscosity can be defined as

$$\nu_T = \frac{\displaystyle\int_{\mathscr{D}} \overline{u_i^{SS} u_i^{SS}}\, \mathrm{d}x_2}{\left(\mathscr{D} \displaystyle\int_{\mathscr{D}} \overline{\frac{\partial u_i^{SS}}{\partial x_j}} \overline{\frac{\partial u_i^{SS}}{\partial x_j}}\, \mathrm{d}x_2 \right)^{1/2}}. \tag{B 4}$$

The integrals over x_2 are used to eliminate the inhomogeneous direction since ν_T should not be a function of this direction. In equation (B 4), the term

$$-\tfrac{1}{3}\delta_{ij}(\overline{\overline{u_k}^{SS}\overline{u_k}^{SS}}^{SS} - \overline{\overline{\overline{u_k}^{SS}\overline{u_k}^{SS}}^{SS}})$$

has been dropped because it can be combined with the pressure term which has been dropped in this analysis (see § 3.3). This representation is simpler than that of Aubry *et al.* (1988) since it was necessary in that study to keep the pressure term, but is the same as that of Glauser *et al.* (1989).

Utilizing the relationships of (2.4) and (3.10), the following expression arises:

$$\nu_T = \frac{\displaystyle\sum_{k_1,k_3,n} \lambda^{(n)}_{k_1,k_3}}{\left(\mathscr{D} L_1 L_3 \displaystyle\sum_{k_1,k_3,n} \lambda^{(n)}_{k_1,k_3} \left(\int_{-L_2}^{L_3} \frac{\mathrm{d}\Phi^{(n)}_{i_{k_1,k_3}}}{\mathrm{d}y} \frac{\mathrm{d}\Phi^{*(n)}_{i_{k_1,k_3}}}{\mathrm{d}y} \mathrm{d}y - 4\pi^2(k_1^2 + k_3^2) \right) \right)^{1/2}}, \tag{B 5}$$

where the sum $\sum_{k_1,k_3,n}$ corresponds only to the first neglected modes.

REFERENCES

Aubry, N., Holmes, P., Lumley, J. L. & Stone, E. 1988 The dynamics of coherent structures in the wall region of a turbulent boundary layer. *J. Fluid Mech.* **192**, 115–173.

Aubry, N., Lumley, J. L. & Holmes, P. 1990 The effect of modeled drag reduction on the wall region. *Theoret. Comput. Fluid Dyn.* **1**, 229–248.

Berkooz, G. 1992 Feedback control of boundary deformation of models of the turbulent wall layer. *Rep.* FDA-92-16. Cornell University.

Berkooz, G., Holmes, P. & Lumley, J. L. 1991 Intermittent dynamics in simple models of the turbulent wall layer. *J. Fluid Mech.* **230**, 75–95.

Berkooz, G., Holmes, P. & Lumley, J. L. 1993*a* The Proper Orthogonal Decomposition in the analysis of turbulent flows. *Ann. Rev. Fluid Mech.* **25**, 539–575.

Berkooz, G., Holmes, P. & Lumley, J. L. 1993*b* On the relation between low-dimensional models and the dynamics of coherent structures in turbulent wall layers. *Theoret. Comput. Fluid Dyn.* **4**, 255–269.

Bonnet, J.-P., Cole, D. R., Delville, J., Glauser, M. N. & Ukeiley, L. S. 1994 Stochastic estimation and proper orthogonal decomposition: Complementary techniques for identifying structure. *Exps. Fluids* **17**, 307–314.

Boussinesq, T. V. 1877 Théorie de l'écoulement tourbillonnant. *Mém. Pré. par div. Sav. Paris*, **23**.

Citriniti, J. H. 1996 Experimental investigation into the dynamics of the axisymmetric mixing layer utilizing the Proper Orthogonal Decomposition. PhD thesis, State University of New York at Buffalo.

Cordier, L. 1996 Etude de systèmes dynamiques basés sur la décomposition orthogonale aux valeurs propres (POD). Application à la couche de mélange turbulente et à l'écoulement entre deux disques contra-rotatifs. PhD thesis, University of Poitiers.

Delville, J. 1995 La décomposition orthogonale aux valeurs propres et l'analyse de l'organisation tridimensionnelle des écoulements turbulents cisaillés libres. PhD thesis, University of Poitiers.

Delville, J., Ukeiley, L. S., Cordier L., Bonnet, J.-P. & Glauser, M. N. 1999 Examination of

https://doi.org/10.1017/S0022112001004803 Published online by Cambridge University Press

large-scale structures in a turbulent plane mixing layer. Part 1. Proper orthogonal decomposition. *J. Fluid Mech.* **391**, 91–122.

Doedel, E. J., Keller, H. & Kernevez J. P. 1991 Numerical analysis and control of bifurcation problems. *Intl J. Bifurcation Chaos* **1**, 493–520.

George, W. K. 1988 Insight into the dynamics of coherent structures from a Proper Orthogonal Decomposition. In *Symp. on Near Wall Turbulence, Dubrovnik, Yugoslavia, May 16–20* (ed. S. J. Kline & N. H. Afgan). Hemisphere.

Glauser, M. N. 1987 Coherent structures in the axisymmetric turbulent jet. PhD thesis, State University of New York at Buffalo.

Glauser, M. N. & George, W. K. 1992 Application of multipoint measurements for flow characterization. *Expl Therm. Fluid Sci.* **5**, 617–632.

Glauser, M. N., Zheng, X. & Doering C. R. 1989 The dynamics of organized structures in the axisymmetric jet mixing layer. In *Turbulence and Coherent Structures* (ed. O. Metais & M. Lesieur). Kluwer.

Glauser, M. N., Zheng, X. & George, W. K. 1990 The streamwise evolution of coherent structures in the axisymmetric jet mixing layer. In *Recent Developments in Turbulence* (ed. T. B. Gatski, S. Sarkar & C. G. Speziale). Springer.

Herzog, S. 1986 The large-scale structure in the near-wall of turbulent pipe flow. PhD thesis, Cornell University.

Hinze, J. O. 1975 *Turbulence*. McGraw-Hill.

Holmes, P., Lumley, J. L. & Berkooz, G. 1996 *Turbulence, Coherent Structures, Dynamical Systems and Symmetry*. Cambridge University Press.

Lorenz, E. N. 1963 Deterministic non-periodic flow. *J. Atmos. Sci.* **20**, 130–141.

Lumley, J. L. 1967 The structure of inhomogeneous turbulent flows. In *Atmospheric Turbulence and Radio Wave Propagation* (ed. A. M. Yaglom & V. I. Tatarsky), pp. 166–178. Nauka, Moscow.

Lumley, J. L. 1970 *Stochastic Tools in Turbulence*. Academic.

Metcalfe, R. W., Orszag, S. A., Brachet, M. E., Menon, M. & Riley, J. J. 1987 Secondary instability of a temporally growing mixing layer. *J. Fluid Mech.* **184**, 207–243.

Michalke, A. 1964 On the inviscid instability of the hyperbolic-tangent velocity profile. *J. Fluid Mech.* **19**, 543–556.

Pierrehumbert, R. T. & Widnall, S. E. 1982 The two- and three-dimensional instabilities of a spatially periodic shear layer. *J. Fluid Mech.* **114**, 59–82.

Poje, A. C. & Lumley, J. L. 1995 A model for large-scale structures in turbulent shear flows. *J. Fluid Mech.* **285**, 349–369.

Rajaee, M., Karlsson, S. & Sirovich, L. 1994 Low-dimensional description of free-shear-flow coherent structures and their dynamical behaviour. *J. Fluid Mech.* **258**, 1–29.

Rempfer, D. 1995 Investigations of boundary layer transition via Galerkin projections of empirical eigenfunctions. *Phys. Fluids* **8**, 175–188.

Rempfer, D. 2000 On low-dimensional Galerkin models for fluid flow. *Theoret. Comput. Fluid Dyn.* **14**, 75–88.

Rempfer, D. & Fasel, H. F. 1994 Evolution of three-dimensional coherent structures in a flat-plate boundary layer. *J. Fluid Mech.* **260**, 351–375.

Ruelle, D. & Takens, F. 1971 On the nature of turbulence. *Commun. Math. Phys.* **20**, 167–192.

Sanghi, S. & Aubry, N. 1993 Mode interaction models for near-wall turbulence. *J. Fluid Mech.* **252**, 239–264.

Ukeiley, L. S. 1995 Dynamics of large-scale structures in a plane turbulent mixing layer. PhD thesis, Clarkson University.

Wick, D. P., Glauser, M. N. & Ukeiley, L. S. 1994 Investigation of turbulent flows via Pseudo Flow Visualization. Part 1. Axisymmetric jet mixing layer. *Expl Therm. Fluid Sci.* **9**, 391–404.

Zheng, X. & Glauser M. N. 1991 A low-dimensional dynamical systems description of coherent structures in the axisymmetric jet mixing layer. *Rep.* MAE-247. Clarkson University.

Zhou, X. & Sirovich, L. 1992 Coherence and chaos in a model of turbulent boundary layer. *Phys. Fluids* A **4**, 2855–2874.

https://doi.org/10.1017/S0022112001004803 Published online by Cambridge University Press